

THE TAURUS TUNABLE FILTER FIELD GALAXY SURVEY: SAMPLE SELECTION AND NARROWBAND NUMBER-COUNTS

D. Heath Jones¹

Research School of Astronomy and Astrophysics, Australian National University, Mount Stromlo Observatory, Cotter Road, Weston ACT 2611, Australia

Joss Bland-Hawthorn

Anglo-Australian Observatory, P.O. Box 296, Epping NSW 2121, Australia;
jbh@aaoepp.aao.gov.au

ABSTRACT

Recent evidence suggests a falling volume-averaged star-formation rate (SFR) over $z \lesssim 1$. It is not clear, however, the extent to which the selection of such samples influences the measurement of this quantity. Using the TAURUS Tunable Filter (TTF) we have obtained an emission-line sample of faint star-forming galaxies over comparable lookback times: the *TTF Field Galaxy Survey*. By selecting through emission-lines, we are screening galaxies through a quantity that scales directly with star-formation activity for a given choice of initial mass function. The scanning narrowband technique furnishes a galaxy sample that differs from traditional broadband-selected surveys in both its volume-limited nature and selection of galaxies through emission-line flux. Three discrete wavelength intervals are covered, centered at H α redshifts $z = 0.08, 0.24$ and 0.39 .

Galaxy characteristics are presented and comparisons made with existing surveys of both broadband and emission-line selection. Little overlap is found in a direct comparison between the *TTF Field Galaxy Survey* and a traditional galaxy redshift survey, due to the respective volume and flux limitations of each. When the number-counts of emission-line objects are compared with those expected on the basis of existing H α surveys, we find an excess of ~ 3 times at the faintest limits. While these detections are yet to be independently confirmed, inspection of the stronger subsample of galaxies detected in both the line and continuum (line-on-continuum subsample; 13%) is sufficient to support an excess population. The faintest objects are galaxies with little or no continuum, rendering them undetectable by conventional redshift surveys. This increase in the emission-line field population implies higher star-formation densities over $z \lesssim 0.4$. However, further study in the form of multi-object spectroscopic follow-up is necessary to quantify this and confirm the faintest detections in the sample.

¹*Current Address.* European Southern Observatory, Casilla 19001, Santiago 19, Chile; hjones@eso.org

Subject headings: galaxies: evolution — galaxies: luminosity function, mass function
— instrumentation: Fabry-Perot interferometers

1. INTRODUCTION

The decline in average star-formation rate provides a fundamental constraint to hierarchical models of galaxy formation, over half the age of the universe. Using the TAURUS Tunable Filter (TTF) on the Anglo-Australian Telescope (AAT) we have obtained an emission-line sample of faint star-forming galaxies over half the age of the universe. This *TTF Field Galaxy Survey* (Jones 1999) is primarily sensitive to star-forming galaxies seen through $H\alpha$ at three discrete wavelength intervals, corresponding to redshifts $z = 0.08, 0.24$ and 0.39 . In selecting through emission-lines, we are using a quantity that scales directly with star-formation rate, effectively selecting galaxies by precisely the parameter we aim to measure. By scanning with wavelength, we automatically define a strict volume-limited sample, less affected by the magnitude-volume sampling effects of conventional broadband surveys. Thus, the tunable filter technique provides a unique means of quantifying the star-formation activity across redshifts relevant to interpretation of the most recent star-formation history of the universe.

The red TAURUS Tunable Filter is a tunable Fabry-Perot Interferometer covering 6500–9600 Å (Bland-Hawthorn & Jones 1998a,b). The spacing between the TTF plates is much narrower and adjustable over a wider range than conventional etalons, thereby giving its function as a tunable narrow passband. In effect, the TTF affords monochromatic imaging with an adjustable passband of between 6 and 60 Å. TTF has an important advantage in the detection of faint line emission over conventional redshift surveys. Deep pencil-beam surveys typically pre-select objects down to $B \sim 24$ (Glazebrook *et al.* 1995) or $I \sim 22$ (Lilly *et al.* 1995), since these represent the practical spectroscopic limits on the 4 meter telescopes used. However, these limits are set assuming the objects are dominated by continuum. Objects with continuum flux beyond the spectroscopic limit but with emission-lines above the limit could be detected by these same instruments, albeit through the lines alone. However, because the initial selection is made from the broadband flux, such objects are excluded *at the outset* on the basis of having too faint a continuum level.

In order to match TTF, a broadband-selected redshift survey needs to select objects to a fainter limit, in the knowledge that for the faintest objects, only those with emission-lines will register a detection spectroscopically. However, this represents a vastly inefficient way of finding emission-line galaxies. Between $B \sim 24$ and $B \sim 28$, the number of objects on the sky (per magnitude interval) increases by an order of magnitude (Metcalf *et al.* 1995). Such object densities would be impractical to search given the limitations of current multi-slit spectrographs in terms of object multiplex. In this paper we compare the very different emission-line galaxy samples obtained by the *TTF Field Galaxy Survey* and the Autofib Galaxy Redshift Survey (Ellis *et al.* 1996) in regions

where the two overlap.

In this paper we describe the *TTF Field Galaxy Survey*. Section 2 discusses the adopted survey strategy and the reasons for this approach. Section 3 describes the selection of the main emission-line sample and its attributes. Known selection effects and potential sources of contamination are reviewed and their effect on the sample discussed. The main characteristics of the sample measurable from these TTF data are given in Sect. 4. Included in this section are narrowband number-counts and a comparison of our narrowband selected emission-line galaxies with those of the broadband-selected Autofib Galaxy Redshift Survey. We also derive preliminary $H\alpha$ luminosity functions and compare them to those of existing surveys. Concluding remarks are made in Sect. 5. Unless stated otherwise, we assume a Friedmann model cosmology (cosmological constant $\Lambda_0 = 0$) with a Hubble constant $H_0 = 50 \text{ km s}^{-1} \text{ Mpc}^{-1}$ and deceleration parameter $q_0 = 0.5$.

2. SURVEY STRATEGY

2.1. Survey Coverage

Considerable freedom exists in a scanning narrowband survey conducted with a tunable filter, by virtue of the flexibility of the instrument. The elements that remain fixed are field coverage on the sky and the Airy-profile shape of the passband. The adjustable parameters are the passband width, the passband coverage and sampling rate with wavelength, and the exposure time per slice. Individually, each affects the number of objects obtained and a judicious selection is necessary if sample size is to be maximized.

The *TTF Field Galaxy Survey* is a survey for redshifted emission-line galaxies in the field. All fields were taken with TTF in TAURUS-2 at the $f/8$ Cassegrain focus of the Anglo-Australian Telescope (AAT). The survey comprises 15 scans of 10 slices, at random high-galactic latitude fields scattered around the sky. By *slice*, we mean an exposure at a particular wavelength, or the image obtained by co-adding many such exposures. The total sky coverage is 0.27 ° with most fields selected on the celestial equator for maximum accessibility from both northern and southern observatories. The scans are distributed between the 707/26 (R_1), 814/33 (R_5) and 909/40 (R_8) TTF blocking filters. Each scan was repeated 3 times with the telescope offset by $\sim 10''$ between each so that cosmic-rays and ghost images could be removed through median filtering. Two CCDs were used: a 4096×2048 pix MIT-LL and a 1024×1024 pix Tektronix with pixel scales of 0.371 and $0.594 \text{ '' pix}^{-1}$ respectively at AAT $f/8$. In both cases, individual fields were limited by a circular field stop of $9'$ diameter.

Table 1 summarizes the passband settings as used for scans in each spectral region. Mean passbands with FWHM ($\delta\lambda$) of 12.9, 16.4 and 22.3 \AA were used to cover 707/26, 814/33 and 909/40 respectively. In velocity space the passbands had widths of 548, 604 and 725 km s^{-1} respectively. We would have preferred to maintain a fixed velocity width between wavelength windows although

this proved difficult in practice since many of the TTF spectral regions were being wavelength-calibrated for the very first time during these observations. Passbands were stepped in increments of $1.3\delta\lambda$ as a compromise between velocity coverage and sampling continuity.

Table 2 gives the observational characteristics for scans in each of the three spectral regions, in terms of $H\alpha$ and [O II]. For $H\alpha$, the spectral regions sample redshift windows at $z = 0.08, 0.24$ and 0.39 . Note that the passbands used include the contribution of nearby [N II] emission with $H\alpha$. Corresponding redshifts in the [O II] line are $z = 0.90, 1.18$ and 1.47 , although we expect fewer [O II] galaxies at our flux limits. We attempted to compensate somewhat for the increased volume (per scan) represented at higher redshifts and longer wavelengths. As such, 7 fields were scanned in the 707/26 filter, 5 in the 814/33 and 3 in the 909/40. This arrangement provided approximately equal volumes in [O II] ($\sim 48000 \text{ Mpc}^3$) but a large range in $H\alpha$ ($1000 - 10000 \text{ Mpc}^3$), because of the low $H\alpha$ redshift for the 707/26 window. The only way to match the low and high redshift volumes in an efficient manner would be through a wide-field instrument such as an objective prism on a Schmidt telescope. However, these are typically 6 magnitudes less-sensitive than TTF in the case of photographic surveys (e.g. Zamorano *et al.* 1994) and 4 magnitudes with the use of a CCD (Salzer *et al.* 2000). For wide-field tunable filter searches, the main limitation is the degradation of bandpass transmission that an interference device such as a tunable filter experiences in the fast beam of a wide-field instrument (Lissberger & Wilcock 1959). Bland-Hawthorn *et al.* (2001) describe the design of a wide-field tunable Lyot filter that avoids these difficulties.

Exposure times were typically 600 s per slice for the 707/26 and 814/33 scans and 1080 s per slice for the 909/40 scans. Of the 13 nights obtained on the Anglo-Australian Telescope (AAT) during 1997 April – 1998 April, 7 were photometric with reliable flux measurements. Only scans taken under photometric conditions have been included. These exposure limits permit us to reach $0.5 \times 10^{-16} \text{ erg s}^{-1} \text{ cm}^{-2} \text{ band}^{-1}$ as a 3σ -detection in a $2''$ aperture, in our deepest exposures for the 909/40 interval. For a 20 \AA bandpass, this flux is equivalent to $2.5 \times 10^{-18} \text{ erg s}^{-1} \text{ cm}^{-2} \text{ \AA}^{-1}$ or $I = 21.8$ as broadband continuum. Alternatively, if the $0.5 \times 10^{-16} \text{ erg s}^{-1} \text{ cm}^{-2} \text{ band}^{-1}$ is confined solely to a *line*, (with no other continuum), then this is equivalent to a broadband detection limit of $I = 26.8$. The instantaneous star-formation rate (SFR) scales directly with the $H\alpha$ and [O II] line luminosity. Using the calibrations for $H\alpha$ and [O II] from the literature review of Kennicutt (1998) we can determine the limiting star-formation rates of our sample. A limiting flux detection of $\sim 0.5 \times 10^{-16} \text{ erg s}^{-1} \text{ cm}^{-2} \text{ band}^{-1}$ is sufficient to detect and measure star-formation rates of a few tenths $M_{\odot} \text{ yr}^{-1}$, comparable with SMC-type levels at the nearest redshifts and the LMC at $z_{H\alpha} \sim 0.4$.

The narrowband scanning of TTF selects a galaxy sample that differs in two important ways from conventional redshift surveys. First, the narrowband technique produces a *volume-limited* sample of emission-line galaxies. The volume of redshift space covered is chosen by the observer through the range and placement of narrowbands. This differs from the broadband limit of conventional redshift surveys which allows galaxies from a wide range in redshift, making total volume a complex function of redshift. The second difference is that TTF selects objects through narrowband

flux which is sensitive to the line flux and therefore star-formation rate. Most conventional redshift surveys define emission-line sub-samples from the initial broadband-selected sample. The inclusion of a galaxy in such samples is dictated by the continuum of the combined stellar population and not by the instantaneous star-formation rate. To define a complete star-forming sample over a given volume, a narrow bandpass well-matched to flux detection in an emission-line is essential.

Since the TTF technique is without precedent we directed 9 of our fields to include emission-line galaxies found as part of the Autofib galaxy redshift catalogue (Ellis *et al.* 1996). The Autofib catalogue contains over 1700 galaxies in the apparent magnitude range $11.5 < b_J < 24.0$. Since it is the combination of many optical surveys, emission-line galaxies are detected primarily through [O II]. Of the TTF fields observed, there are 18 emission-line galaxies in the Autofib catalogue with redshifts placing H α in one of either the 707/26, 814/33 or 909/40 blocking filters. We defined the Autofib emission-line sample as those galaxies with [O II] rest-frame equivalent widths (REWs) greater than 10 Å. Through the galaxies common to both catalogues, we can examine how representative a broadband-selected survey is of the underlying star-forming population. Furthermore, we can gain insight into how the TTF detection rate goes as a function of broadband magnitude.

Table 3 shows the observations undertaken for the *TTF Field Galaxy Survey*. The number of Autofib galaxies expected in H α is also included. Figure 1 shows the distribution of fields on the sky. The fields overlapping with the Autofib galaxies are indicated. We made a search of the NASA Extragalactic Database² (NED) to check whether any known clusters lie near our fields. No clusters with measured redshifts overlap with our fields although 4 of the optically-identified cluster candidates of Lidman & Peterson (1996) lie within 6' radius of our 10_3F, 13_3E, 10_3C and 10_3H field centres. Within the Lidman & Peterson sample, these cluster candidates are all rated with low significance. However, we later examine the number density and wavelength distribution of emission-line candidates within these fields as a check.

2.2. Background Source Contamination

All narrowband imaging emission-line searches are open to different lines at varying redshift. Any line for which both the rest wavelength and source redshift act to place it within a TTF survey interval will be detected if sufficiently luminous. The fixed flux detection limit translates to different limiting luminosities in each emission-line, depending on its redshift. Furthermore, the fixed wavelength coverage of the scan defines different co-moving volumes at each of the redshifts. This needs to be taken into account when optimising survey coverage, not just in terms of object density, but also in the *type* of emission-lines sought, since some are preferred to others for measuring star-formation rates (Kennicutt 1992a, 1998).

² Operated by the Jet Propulsion Laboratory, California Institute of Technology, under contract with the National Aeronautics and Space Administration.

In a blind search at these wavelengths the emission-lines we would most expect to see in galaxies are $H\alpha$, $[O II]$, $H\beta$ and $[O III]$ (Tresse *et al.* 1999; Folkes *et al.* 1999; Kennicutt 1992b). The TTF passband is too wide to separate $H\alpha$ and at least one of $[N II]$ $\lambda\lambda 6548,6583$. The detection of $Ly\alpha$ would be rare at the levels we are probing. Recent estimates for the density of $Ly\alpha$ emission-line galaxies with line fluxes of 3 to 5×10^{-17} $\text{erg s}^{-1} \text{cm}^{-2}$ number $\sim 4000 \text{ Mpc}^{-1}$ per unit z (Rhoads *et al.* 2000). This implies negligible numbers of $Ly\alpha$ -emitters at our brighter flux limit ($\sim 1 \times 10^{-16}$ $\text{erg s}^{-1} \text{cm}^{-2}$). $[S II]$ $\lambda\lambda 6717,6731$ is another line we do not expect to find since it is are too far into the red to be found in an appreciable volume. In any narrowband survey, we expect a competing luminosity-volume effect between $H\alpha$ being probed to fainter luminosities over smaller volumes, and background emission-lines at brighter luminosities but larger volumes.

$H\alpha$ is the most preferred line for measuring the instantaneous star-formation rate, being the strongest Balmer recombination line and in the part of the optical spectrum affected least by extinction (Kennicutt 1992a; van der Werf 1997; Tresse & Maddox 1998; Glazebrook *et al.* 1999). It is directly related to the number of short-lived OB stars, indicative of the stellar birthrate in a galaxy. These hot, massive stars produce ultraviolet (UV) radiation that ionises the nearby gas to create an H II region. Recombination produces the observed emission-lines and of these, $H\alpha$ most closely traces the amount of ionising UV flux. Of the other Balmer lines, $H\beta$ is weaker and prone to filling-in by the underlying stellar absorption. $[O II]$ can be also be related to the instantaneous star-formation rate, although the underlying assumptions are less robust, since this (and other lines such as $[N II]$, $[O III]$ and $[S II]$), depend heavily on the metal fraction of the gas (Kennicutt 1992a). In the case of lines with a higher ionisation potential, the energy of the incident UV flux is also an important factor. As a consequence, they are unreliable star-formation indicators. Of all the optical lines, $H\alpha$ is the preferred choice.

Given the reasons outlined above, $H\alpha$ is the obvious target for our survey of star-formation. However, it is prudent for us to examine the numbers of background emission-line galaxies likely from a scanning narrowband survey. Accordingly we made estimates of the galaxy numbers expected from each of the other major optical emission lines relative to $H\alpha$. For a Friedmann model cosmology with $\Lambda_0 = 0$, the co-moving volume of space sampled in an emission-line at redshift z , is

$$\Delta V = \frac{4\pi d_M^2 c \Delta z A_{\text{field}}}{1.4851 \times 10^8 \cdot H_0(1+z)(1+\Omega_0 z)^{1/2}}. \quad (1)$$

Here, A_{field} is the area of the field on the $1.4851 \times 10^8 \text{ Mpc}^2$ of the sky and Δz is the redshift coverage of the scan and d_M is the proper distance. Galaxy emission-line luminosity functions have been determined by several authors for $H\alpha$ at a range of redshift (Gallego *et al.* 1995; Tresse & Maddox 1998; Gronwall 1998; Yan *et al.* 1999). In most of these cases, the $H\alpha$ luminosity function is found to be well-matched by a Schechter (1976) function,

$$\phi(L) dL = \phi^* (L/L^*)^\alpha \exp(-L/L^*) d(L/L^*), \quad (2)$$

where $\phi(L)$ is the number of galaxies per unit volume at luminosity L . The parameters ϕ^* , L^* and α are constants describing the shape of the distribution. More specifically, the density of $H\alpha$

galaxies per unit volume, $\Phi[\log(L_{\text{H}\alpha})]$, is binned per 0.4 interval in $\log(L_{\text{H}\alpha})$, and can be related to the Schechter description through

$$\Phi \left[\log(L_{\text{H}\alpha}) \right] \frac{d \log L_{\text{H}\alpha}}{0.4} = \phi(L_{\text{H}\alpha}) dL_{\text{H}\alpha}, \quad (3)$$

for $L = L_{\text{H}\alpha}$, luminosity in H α (Gallego *et al.* 1995). The total number $N(L_{\text{lim}})$ of H α emission-line galaxies (per unit volume) detected to limiting luminosity L_{lim} can be obtained by integrating Eqn. (2) to that luminosity,

$$\begin{aligned} N(L_{\text{lim}}) &= \int_{L_{\text{lim}}}^{\infty} \phi(L_{\text{H}\alpha}) dL_{\text{H}\alpha} \\ &= \phi^* \Gamma(\alpha + 1) \cdot [1 - P(\alpha + 1, L_{\text{lim}}/L^*)]. \end{aligned} \quad (4)$$

Here, $P(\alpha + 1, L_{\text{lim}}/L^*)$ is the incomplete gamma function³ evaluated in terms of the Schechter parameters. We applied the function in Eqn. (4) to estimate the total numbers of H α emission-line galaxies seen in each of the TTF scan intervals. As the H α luminosity function evolves rapidly with redshift, we assumed an evolving ϕ^* , L^* and α of the forms

$$\begin{aligned} \phi^*(z) &= \phi_0^* (1 + z)^{\gamma_\phi}, \\ L^*(z) &= L_0^* (1 + z)^{\gamma_L}, \\ \alpha(z) &= \alpha_0 + \gamma_\alpha z, \end{aligned} \quad (5)$$

following the forms adopted by Heyl *et al.* (1997) for evolution in the broadband luminosity function. The free parameters ϕ_0^* , L_0^* , α_0 , γ_ϕ , γ_L and γ_α were constrained by the luminosity functions of Gallego *et al.* (1995) at $z = 0$ ($\phi^* = 0.63 \times 10^{-3} \text{ Mpc}^{-3}$, $L^* = 10^{42.15} \text{ erg s}^{-1}$, $\alpha = -1.3$) and Tresse & Maddox (1998) at $z = 0.2$ ($\phi^* = 1.48 \times 10^{-3} \text{ Mpc}^{-3}$, $L^* = 10^{42.13} \text{ erg s}^{-1}$, $\alpha = -1.35$). Table 4 lists the parameters describing our adopted H α luminosity function evolution, as constrained by these two samples.

With no equivalent emission-line luminosity functions for lines of [O II], H β and [O III], our best approach is to scale the H α luminosities by the mean line flux ratios of Kennicutt (1992a). Kennicutt deliberately selected his sample of E-Irr galaxies to match the mix of morphological types seen in the Revised Shapley-Ames (RSA) Catalog (Sandage & Tammann 1981). As such, it can not be considered to be representative of the true space density these types.⁴ Accordingly, we computed mean flux ratios for [O II], H β , [O III], [S II] and [N II] weighting Kennicutt’s galaxy types by their occurrence. Measurements of ϕ^* by Heyl *et al.* (1997) were used to estimate the relative space densities of different types and their evolution with redshift. Figure 2 shows that under such a weighting scheme, all line ratios show little change out to $z \sim 1$. This is consistent

³ By definition, the incomplete gamma function is $P(a, x) = \int_0^x e^{-t} t^{a-1} dt / \Gamma(a)$, where $\Gamma(a)$ is the gamma function and $a > 0$.

⁴ For example, the RSA Catalog under-represents the true space density of Sd and later types due to their fainter mean absolute magnitudes compared to early-type galaxies (Sandage & Tammann 1981).

with Glazebrook *et al.* (1999) who find broad agreement between the $\text{H}\alpha/[\text{O II}]$ ratios of their $z \sim 1$ sample and the local Kennicutt (1992a) sample. The greatest change is the sharp decrease in $[\text{N II}]/\text{H}\alpha$ ratios over $z \lesssim 0.2$. We suspect this is due to the steep decline in the numbers of early-type galaxies (Fig. 2, *inset*), in which strong $[\text{N II}]$ emission is most prevalent (Phillips *et al.* 1986). This constancy in line flux ratios is indeed what we might expect, given a field population composed almost exclusively of star-forming galaxies at such lookback times (e.g. Ellis *et al.* 1996; Tresse *et al.* 1999). The effects of extinction aside, line ratios will only exhibit significant variation in cases of active galactic nuclei (Kennicutt 1992a), for which Sarajedini *et al.* (1999) find no density evolution over $z < 0.4$ and mild evolution between $z = 0.4$ and $z = 0.8$.

Figure 3 shows the relative predicted numbers that our calculations yield for each of the 707/26, 814/33 and 909/40 TTF spectral windows. Numbers are shown as a function of flux for both individual flux bins (Fig. 3, *left*) and cumulatively with decreasing flux (Fig. 3, *right*). We have assumed the galaxies to have a mean internal extinction of 1 mag at $\text{H}\alpha$ and a mean $\text{H}\alpha/(\text{H}\alpha+[\text{N II}])$ flux ratio of 0.69 (Tresse & Maddox 1998). Note however that both Tresse & Maddox and Tresse *et al.* (1999) find a trend in $[\text{N II}]$ flux against $\text{H}\alpha$. We have not included this in the correction, since both surveys use slit spectroscopy (1.75" and 8" slits respectively) which misses light from the outer regions of large galaxies in a way that narrowband imaging does not.

The flux limits of our raw sample are ~ 0.5 to 1×10^{-16} $\text{erg s}^{-1} \text{cm}^{-2}$. As expected, $\text{H}\alpha$ galaxies dominate the cumulative numbers at the brightest fluxes because background galaxies in the other lines need to be intrinsically more luminous, and hence, much rarer objects. At the fainter fluxes, we find a broader mix of emission-lines as the larger volumes sampled for the background lines begin to balance the fainter luminosity limits probed in $\text{H}\alpha$.

Around the flux limits of our survey, $\text{H}\alpha$ dominates over $[\text{O II}]$ thereby representing more than 90% of the full emission-line sample in the redder 814/33 and 909/40 bands. In the 707/26 band, the $\text{H}\alpha$ and $[\text{O II}]$ galaxies comprise approximately equal numbers ($\sim 50\%$) with comparatively fewer numbers of galaxies seen in $[\text{O III}]$ and $\text{H}\beta$. The dominance of $\text{H}\alpha$ at stronger fluxes in all bands suggests that samples restricted to these values will essentially constitute $\text{H}\alpha$, with little contamination from background $[\text{O II}]$. In the case of 707/26, this means truncating the emission-line sample artificially higher (~ 1.5 to 2×10^{-16} $\text{erg s}^{-1} \text{cm}^{-2}$) than the natural flux limits of the survey. The trade-off is that there are far fewer galaxies with higher line fluxes. In short, we expect to $\text{H}\alpha$ galaxies to dominate samples at fluxes exceeding $\sim 2 \times 10^{-16}$ $\text{erg s}^{-1} \text{cm}^{-2}$ for the 707 interval, and $\sim 0.5 \times 10^{-16}$ $\text{erg s}^{-1} \text{cm}^{-2}$ for the 814 and 909 intervals.

3. EMISSION-LINE SAMPLE

3.1. Candidate Selection

The observations were reduced as follows. Individual frames were bias-subtracted and divided by flatfields. Night-sky rings were removed and images aligned and co-added in three separate scans. Object detection and measurement was undertaken using *SExtractor* (Bertin & Arnouts 1996). Objects were detected from the original frames and subsequently photometered from a matching set of frames degraded to match the worst seeing frame. Cosmic-ray and ghost image catalogues were constructed for each scan and used to remove these detections from the raw emission-line candidate catalogues. Emission-line candidates in which line flux was detected and continuum was not were selected by the line detections appearing in one or two adjacent frames and no others. These we term our *line-only* candidates. Candidates showing line flux on an otherwise detectable continuum we call our *line-on-continuum* candidates. These were found through a more complex procedure. Initially, all objects in the field with continuum detected in 5 or more frames had a straight-line of best-fit iteratively fit to the continuum flux with wavelength. Fluxes deviant from this fit were rejected on successive iterations refining the fit. Any objects showing flux deviations in one or two adjacent frames above the flux uncertainties of the continuum were included in the emission-line catalogue. All objects in this group (in excess of ~ 200) were inspected on a mosaic of postage-stamp images (through the scan) to confirm the rejection of cosmic-rays and ghosts. The quality of the deviation above the fit was also checked to confirm the fit as true to the continuum and unaffected by bad data points. The continuum and emission-line fluxes in both sets were calibrated through standard star observations from the same nights. Measured fluxes were corrected for extinction by our own galaxy (albeit small since the fields were all at high galactic latitude) and for flux truncation by the apertures where necessary. The specific procedures are described by Jones (1999).

Figure 4 shows example scans and TTF spectra for a subset of candidates from one of the *TTF Field Galaxy Survey* fields. All of the objects shown are line-on-continuum candidates, for which the continuum flux has been fit in order to find the emission. Preliminary and final continuum fits are shown in the spectra (*dotted* and *dashed* lines respectively). One object (214.14) is one of the 18 Autofib galaxies within our fields. In detection terms, the relative strength of an emission-line is quantified in terms of its σ -*deviation*. This is the line flux in units of background σ . For line-only candidates, σ is the background RMS of the local sky noise against which the detection was made. For example, a line-only detection with a σ -deviation of 3 is a 3σ -detection in the usual sense. For line-on-continuum candidates, the situation is complicated by the presence of continuum. In this case, the “background σ ” is that determined by either the RMS scatter of fluxes about the continuum fit, or the mean uncertainty in the continuum fluxes, whichever is greatest. Hence, objects with strong emission flux might be rated with a low σ -deviation if that emission is superposed on a continuum of comparable or greater strength. The σ -deviation is an expression of the ease with which an emission-line was detected, not its strength in flux.

The raw catalogue of emission-line candidates was selected from all objects with σ -deviations of 3 or greater. At 3σ , those candidates seen as a peak in a single frame ideally require confir-

mation through a follow-up observation such as spectroscopy. Figure 5 shows the distribution of σ -deviations for each field. The line-only detections (*horizontal tickmarks*) and line-on-continuum detections (*crosses*) are shown separately. Observe in Figs. 5(b) and (c) that from the point of view of detection, the majority of candidates ($\gtrsim 50\%$) are weak detections of between 3 and 4σ , as might be expected. Most fields show a similar distribution of σ -deviations with respect to each other. The exception is the 00_3A field which shows substantial numbers of strong σ -deviation objects in both cases of object. We suspect that this may be due to either the field being observed under above-average conditions and/or a possible chance alignment with a galaxy cluster. We also note that this field has comparatively higher numbers of faint line-only detections, consistent with either hypothesis.

Finally, note that there is a systematic offset between the limiting line flux of the line-only sample and its corresponding line-on-continuum sample for the same field. This is simply a reflection of the fact that a 3σ -deviation detection seen against background sky can probe to fainter line levels than an equivalent detection measured against object continuum. These differences in sensitivity under different circumstances must be taken into account when deriving a homogeneous sub-sample of objects.

3.2. Selection of a Homogeneous Sub-Sample

The selection of a homogeneous sub-sample of emission-line candidates across many fields must necessarily take into account several observables simultaneously. There are many factors (both external and intrinsic to an object) that influence its detection probability. By *homogeneous sub-sample*, we mean a sample of emission-line objects that conforms to a set of well-defined selection criteria, within which we know our sample is complete, or near complete. By *complete*, we mean a 100% detection probability for all objects within a given set of selection criteria. The detection probability can be assessed by generating artificial datasets spanning similar object characteristics as the real sample. Since the observational properties of the artificial objects are known from the outset, a success rate for detection can be measured when these objects are passed through the same selection methods as were used for the real objects. This can be used to assess the amount of incompleteness as a function of selection level and make for its correction. In practice, selection cuts are placed at some threshold level, below which, the incompleteness corrections become intolerably large. Corrections for incompleteness are made by weighting object numbers by the known missing fraction, provided the observed galaxy numbers are sufficiently large and the correction factors small.

In the *TTF Field Galaxy Survey*, all objects are first selected on the basis of a detection by *SExtractor*, which becomes increasingly incomplete at the faintest limits. The line-only candidates are subject to this alone whereas the line-on-continuum objects undergo further selection on the basis of line flux relative to continuum. The detection probability of both procedures must be measured before we can set bounds to define a homogeneous sub-sample. The bounds should be

such that we can combine both types of object into a single uniform catalogue, within which the differences in selection method are no longer important. We examined the detection probabilities for the fields observed in cases of worst seeing and/or highest sky background. Images were constructed containing artificial objects under identical conditions of seeing and background RMS as the real observations. The artificial objects populated a 10×10 grid of object sizes and line fluxes across a range of values encompassing those from the real data. Objects of a given size and flux were duplicated 20 times. *SExtractor* was executed on the artificial images using an identical detection configuration as the real field concerned. Its success at finding some fraction of objects at a given size and flux is a measure of the detection probability as a function of both parameters, under the particular observing conditions. In all fields, the detection probability fell away quite steeply from 100% detectability, over a relatively narrow strip along the grid. Two fields (22_3A for 707; 10_3C for 909) showed detection probabilities declining at higher flux levels than the other fields in that group. These two fields also contribute significantly less to the final object numbers. Given this, and the high levels of incompleteness they would impose on the other fields, we excluded them from the homogeneous sub-samples.

Figure 6 shows just the raw line-only detection candidates in terms of both mean detected flux and object size. The mean detected flux for these objects is simply the line flux detected on a single narrowband frame. The samples in Fig. 6 are labeled by blocking filter and the 22_3A (707) and 10_3C (909) candidates have been removed. The solid lines are contours of detection probability for the *single worst field* of each panel, with the 60%-contour emboldened. All other fields have contours at fainter flux levels, not shown on this figure. The significant number of points in the $\lesssim 20\%$ region come from these more sensitive fields, which exhibit completeness to fainter flux levels. The detection contours show that the natural detection limit of a narrowband survey such as this is emission-line surface brightness. Accordingly, we apply two cuts: a minimum line flux cut and a minimum surface brightness cut. Taken together, they select candidates from *all* fields from within the 60% detection contour of the *worst* field. Individually, all fields except the worst are complete to the selection limits imposed by the latter. Note that because this contour only applies to the worst field, Table 5 lists the flux and surface brightness cuts. A value for surface brightness at the object center is inferred from its FWHM and total flux, assuming an exponential disk profile.

In addition to the cuts above, the line-on-continuum objects are subject to further selection based on the strength of the line flux *relative* to the continuum. This is necessary because of the influence that the continuum level can have in determining whether an emission-line is detected, irrespective of line flux. Figure 7 demonstrates how we apply these cuts to the line-on-continuum objects. Initially, we apply identical flux and surface brightness selection for the line-only candidates, since both catalogues depend upon object detection in the first instance (Fig. 7, *left*). Note that in this case, the mean detected flux is the object *continuum*, not the line as in the line-only case. Second, we restrict the line fluxes to the *same* level as the mean detected continuum flux (Fig. 7 *right*, vertical line). This is because the same detected flux cut applies to both the line-only

and line-on-continuum objects, regardless of whether this detected flux is line or continuum. In doing so, we have a uniform cut in line flux across both samples. We must ensure that these flux cuts define a region of near-100% detection probability. This time, the detectability is measured for a sample of artificial objects with both line *and continuum*. A grid of objects with line and continuum values spanning the ranges in Fig. 7 (*right*) was constructed using the same worst-case noise values for Fig. 6. The detection probability as a function of these two parameters was obtained by measuring the success rate of the software in finding such objects. The contours in Fig. 7 (*right*) show levels of detection probability in this space. The artificial objects were assumed to have the sky noise associated with the largest available aperture for the field. As with the real object catalogue, they were only included if the resulting line had a σ -deviation of 3 or greater. The boundary between 2 and 3σ -deviation detections is represented in Fig. 7 (*right*) by the dashed line. This is the locus of points with 3σ line fluxes in the largest aperture. Had we defined emission-line objects at a lower level than 3σ , we would have populated the region above this line with candidates as well. However, in such cases it is difficult to be satisfied that deviations less than 3σ are significant compared to the natural scatter of points about the mean continuum level.

Our third and final cut is that representing the faintest limit to which we can detect line flux relative to continuum. This is an observed equivalent width (EW) cut, and the levels we have chosen are shown by the labeled solid diagonal lines in Fig. 7 (*right*). The definition for equivalent width from narrowband measurements, is

$$\text{EW} = \frac{F_{\text{line}} \cdot \delta\lambda_e}{F_{\text{cont}}}. \quad (6)$$

Here, F_{line} and F_{cont} are the respective line and continuum fluxes and $\delta\lambda_e$ is the effective width of the passband. The effective width, $\delta\lambda_e$, is that width of the rectangular bandpass with equal area to the true passband, $\delta\lambda$, and with 100% peak transmission. They are related through $\delta\lambda_e = \pi \cdot \delta\lambda/2$. The *rest-frame equivalent width* (REW) is that measured in the reference frame of the galaxy. It is related to the observed equivalent width by $\text{REW} = \text{EW}/(1+z)$, where z is the galaxy redshift.

We make equivalent width cuts at a level ensuring that we are complete both in terms of detection probability and 3σ line detections. We know that we could have detected an object anywhere within the boundaries of line and continuum flux, and observed equivalent width. Table 5 lists the equivalent width cuts applied in each case. Also listed are the rest-frame equivalent widths for H α at its redshift in these passbands. We determine our overall sample completeness by comparing the numbers of objects actually observed with those expected over the same selection space. For each object we determined a *completeness weighting factor*, being the reciprocal of the detection probability in the region of that object. Most objects have weighting factors of 1.0 since they lie in the region of 100% detection probability for their respective field. In summing the completeness weights, each object is represented by the numbers we *should* have detected, thereby giving the total number of objects we could have expected for the homogeneous sub-sample. Figure 8 shows the cumulative completeness of the homogeneous sub-samples as a function of flux. Note that since completeness is a function of surface brightness, its decline is not due to flux alone.

However, Fig. 8 demonstrates that all samples are $\sim 93\%$ complete or greater, at the limits we have set. Table 6 gives the breakdown of types for our homogeneous sub-sample, and the total numbers of observed and expected objects.

3.3. Flux Selection of an H α Sub-Sample

Defining homogeneous emission-line samples is insufficient on its own if we wish to characterize the star-formation history of the universe. We expect our line-flux-selected samples to contain a combination of galaxies seen through H α , [O II] and [O III] at a variety of redshifts matching the observed wavelength. However, the conclusions of Sect. 2.2 (in particular, Fig. 3) suggest that at the brightest fluxes, our samples will be dominated by H α emission-line galaxies. The reason for this is as follows. Such fluxes translate into luminosities brighter than L^* in the emission-line luminosity functions for the background galaxies. As a consequence, H α galaxies dominate, being the only set from which the members are significantly sampled beyond L^* . As can be seen in all cases of Fig. 3, the transition from an H α -dominated sample to that inclusive of other lines is quite sharp. This is due to the exponential decline in galaxy numbers for a Schechter luminosity function for luminosities $L > L^*$.

The homogeneous sub-samples in the 814/33 and 909/40 filters have fluxes greater than 0.71 and $0.57 \times 10^{-16} \text{ erg s}^{-1} \text{ cm}^{-2}$ respectively (Table 5). By Fig. 3, we would expect these samples to consist almost entirely of H α emission ($> 90\%$). We define two H α samples for each of the 707/26, 814/33 and 909/40 sets: one derived from the full sample of emission-line objects and the other from the homogeneous sub-sample. They are selected by taking only those galaxies above the flux limit ensuring complete H α selection, as determined by Fig. 3. Table 7 summarizes the flux cuts made and the sizes of the resulting H α samples. The original homogeneous sub-samples in the 814/33 and 909/40 filters remain intact since the original flux limits (0.71 and $0.57 \times 10^{-16} \text{ erg s}^{-1} \text{ cm}^{-2}$ respectively) restrict these samples to H α galaxies almost entirely ($> 90\%$). However, the homogeneous sub-sample in the 707/26 filter has a wider mix of H α , [O II] and [O III] galaxies and so we take our H α sample as those with line fluxes exceeding $1.50 \times 10^{-16} \text{ erg s}^{-1} \text{ cm}^{-2}$. At this level the H α galaxies constitute more than 80% of the total sample. Table 7 also lists the limiting line luminosities for H α flux at the selection limit, at the mean H α redshift in each interval.

Although this dominance of H α at higher flux is fortuitous for the present analysis, future work is necessary to solve redshift ambiguity, in the form of follow-up spectroscopy. Not only does this see the TTF emission-line identified, but the nature of the galaxy emission and its reddening can be revealed through ratios with other emission-lines. Although such follow-up is beyond the scope of this paper, it is the obvious direction for subsequent work on the survey.

An alternative solution to redshift ambiguity was explored in the form of broadband imaging. As the major optical emission-lines are well-separated in wavelength, the corresponding galaxy redshifts separate the broadband colors unambiguously in a color-color plane. This differs from

conventional photometric redshift techniques (see discussion by Koo 1999) in that a *precise* starting point for the redshifts is given through the limited possibilities offered by $H\alpha$ [O II], [O III] or $H\beta$. The disadvantage of this method is that it requires *all* emission-line galaxies (that make it into the final sample) to have sufficient continuum for a broadband detection. As the galaxies from our survey with sufficient continuum are few ($\sim 5\%$), they do not constitute a sample that both meets this criterion and offers sufficient numbers to be useful. Observations representing many hours on a 4 m-class telescope or greater are required, in which case, spectroscopic follow-up becomes an increasingly feasible alternative. We obtained broadband colors for 12 of the 15 *TTF Field Galaxy Survey* fields. The regions were imaged in *BVRI* on the 1.0 m telescope at Siding Spring Observatory, Australia. This yielded usable colors for the subset of our galaxies ($\sim 13\%$) with sufficient continuum ($B \lesssim 21$). Such colors can then be used to solve the galaxy redshift ambiguity. More details on the application and results of this approach are presented by Jones (1999). However, because the brightest galaxies were too few to be useful, this method could not be applied as a redshift discriminant to the *TTF Field Galaxy Survey* as a whole.

4. SAMPLE CHARACTERISTICS

4.1. Autofib Redshift Survey Comparison

We tested the TTF detection of emission-line galaxies against a conventional broadband-selected redshift sample. The Autofib redshift survey (Ellis *et al.* 1996) is a composite sample of 1700 galaxies obtained through the combination of the DARS (Peterson *et al.* 1985), Autofib (Ellis *et al.* 1996), BES (Broadhurst, Ellis & Shanks 1988), LDSS-1 (Colless *et al.* 1990, 1993) and LDSS-2 (Glazebrook *et al.* 1995) samples. Galaxies have been selected from the magnitude range $11.5 < b_J < 24.0$ and the presence of emission is judged through the [O II] line.⁵ The different samples probe different magnitude ranges and areas on the sky. There are 827 members of the Autofib redshift survey that can be classified as emission-line galaxies, defined as such by [O II] rest-frame equivalent widths greater than 10 \AA . Of these, there are 18 within one of our 9 overlap fields at redshifts placing $H\alpha$ within the relevant scan window (707/26, 814/33 or 909/40). We examined the detection success of TTF on these galaxies as a function of both b_J magnitude and [O II] rest-frame equivalent width.

Table 8 summarizes the results. In addition to the TTF detection rate, we show how many of the TTF object detections occurred as line-on-continuum and how many were line alone. Table 8 shows the trend of fainter galaxies ($b_J \gtrsim 21$) becoming $H\alpha$ line-only detections in increasing numbers. This we expect since the narrow TTF passband is optimized for the detection of faint line flux and not faint continuum. There is also the suggestion of a declining detection rate with fainter

⁵The b_J passband is defined by the combined wavelength sensitivities of the Kodak IIIa-J emulsion and a GG385 glass filter.

limiting apparent magnitude, although it is difficult to tell with such small numbers of galaxies. All of the undetected galaxies (except one) lie at $b_J \sim 21.0$. The one fainter $b_J \sim 22.0$ galaxy which was detected, was detected as a line-only detection. We conclude from this that $b_J = 21.0$ is around the limit at which we can detect galaxies in both their line and continuum. Beyond this, line detections dominate. When ranked according to [O II] rest-frame equivalent width, little is seen in the way of TTF detection trends. Again, the small size of the overlap sample is a limitation, particularly because the majority of objects have [O II] emission with low to moderate rest-frame equivalent widths ($10 \lesssim EW \lesssim 40 \text{ \AA}$).

We have assumed here, however, that all galaxies exhibiting [O II] emission will have equally strong H α . Although this is commonly true it is not always the case, and some of the TTF non-detections in Table 8 may have been simply because there was little or no H α . Tresse *et al.* (1999) find a small but significant fraction of the Stromlo-APM Survey (11%) that show [O II] but no H α . They attribute this to strong stellar absorption and do not find such galaxies to be more prevalent at a particular redshift. So an alternative possibility is that Table 8 underestimates the detection success of TTF in some cases. However, this 11% is less than the $\sim 25\%$ of Autofib [O II] galaxies that TTF does not detect. This suggests that an additional factor is responsible, although it is difficult to be certain when such small sample sizes are involved. Tresse *et al.* note that the fraction of their broadband-selected sample seen in emission ($\sim 60\%$) is the same, irrespective of whether emission is defined through the presence of [O II] or H α . Remarkably, they find that the number of galaxies with [O II] and no H α negates the galaxy numbers with H α and no [O II].

Figure 9 shows the relationship between spectral quantities measured around H α by TTF and [O II] by the Autofib survey for the galaxies in common. In panels (a) and (b), we find little correlation between either the H α and [O II] emission-line fluxes or between the corresponding equivalent width measures. We do not see the EW(H α + [N II]) versus EW([O II]) correlation of Kennicutt (1992a) or Tresse *et al.* (1999), probably because this correlation is weak with large scatter and our sample size is small. The large scatter in Fig. 9(b) may also be due to a tendency of spectroscopic equivalent widths to be overestimates at the limits of a broadband-selected sample, as discussed in Sect. 4.2. Either way, our results lend further weight to Kennicutt (1992a) who finds [O II] flux and equivalent width to be loosely connected to the star-formation rate in a galaxy. In Fig. 9(c) we show the relationship between the Autofib b_J magnitudes and the TTF narrowband continuum measurements. There is reasonable agreement between the two with the line of best-fit being

$$b_J = -2.5 \log F(\text{cont}) + 21.81, \tag{7}$$

where b_J is the photographic magnitude and $F(\text{cont})$ is the narrowband continuum in the TTF bandpass ($10^{-16} \text{ erg s}^{-1} \text{ cm}^{-2} \text{ band}^{-1}$). In making the fit we fixed the slope to -2.5 and weighted the points by the $1/\Delta F^2$ continuum photometry uncertainties. The agreement in panel (c) indicates that the scatter in the equivalent width measurements of panel (b) is due primarily to the dispersion in line flux seen in panel (a). Equation (7) implies that the *continuum* detection limit of TTF is about the same as the $b_J = 24.0$ limit of the broadband-selected survey.

There is little overlap between the emission-line selected galaxies found in the the broadband-selected Autofib redshift survey and the *TTF Field Galaxy Survey*. The vast majority of TTF-selected galaxies have continua too faint for inclusion in the broadband catalogue while the redshifts of the Autofib line-emitters are too wide-ranging for the relatively narrow scan windows of TTF. For the galaxies in common, TTF detects the brighter Autofib galaxies ($b_J \lesssim 21$) in both line and continuum while fainter line-emitters are almost exclusively detected in the line alone. While there is good agreement between the redshifts and continuum fluxes measured by TTF and Autofib around $H\alpha$ and [O II], there is considerable scatter between the measurements of line flux and equivalent width. However, much of this dispersion can be attributed to intrinsic differences between the $H\alpha$ and [O II] lines themselves, as seen in the loose correlations between these lines by Kennicutt (1992a) and Tresse *et al.* (1999). Improved insight into the relative merits of TTF over broadband-selected emission-line samples would be obtained through a redshift survey with near-infrared spectra overlapping with the TTF wavelength intervals directly, so that the same emission-line could be observed by each technique.

4.2. Emission-Line Distributions

Previously (Sect. 2) we discussed the need to examine the emission-line distributions with wavelength for signs of clustering. In the case of our $H\alpha$ sub-samples we can interpret the wavelength distributions directly as distributions in redshift space. Figure 10 shows such distributions by field for galaxies in the entire $H\alpha$ sub-sample. No clear clustering is evident, although there are suggestions of peaks in the 14_3A, 22_3A and 13_3B fields. The 22_3A clustering is irrelevant because this field has been excluded from the homogeneous samples used in our final analysis. Certainly we find no strong evidence for clusters in the 10_3C, 10_3F, 10_3H or 13_3E fields which coincide (directionally at least) with the Lidman & Peterson (1996) candidates. Given the limited impact that clustering appears to have on our field samples, we leave them intact as representative samples of the field population. Of greater interest are the fluctuations in the total numbers of $H\alpha$ galaxies between individual fields, particularly in the 707 set, and to a lesser extent in 814. This is due to the high flux cut imposed upon the 707 sample to ensure a sample of $H\alpha$ galaxies. At this level, the numbers of galaxies field-by-field are sufficiently few that fluctuations of this order are inevitable. Such variations are also seen between fields of broadband-selected redshift surveys (cf. redshift spikes in Fig. 3 of Broadhurst, Ellis & Shanks 1988).

For Fig. 10, the peak wavelength of an emission-line was determined through two different methods depending on the nature of the emission. In objects with no continuum, the peak wavelength was that of the slice showing emission, or the mean wavelength if two adjacent slices showed emission. In objects with continuum, the peak wavelength of the most deviant slice, or the mean wavelength of two adjacent deviant slices was used. Mean wavelengths were computed by weighting the wavelengths of individual slices by the line flux in each. The mean flux ratio $H\alpha/(H\alpha+[N II]) = 0.69$ (Tresse & Maddox 1998) was used to adjust $H\alpha$ fluxes for the contribution

of [N II]. In all cases, wavelength corrections were applied to account for the phase effect with object position relative to the optical centre of the Fabry-Perot beam.

Table 9 summarizes the occurrence of emission-lines in one and two slices for the homogeneous sub-sample of candidates. The cases of detection and non-detection of continuum are shown separately. Single-slice emission-lines represent $\sim 50\%$ of objects with continuum, and a much larger fraction ($\sim 98\%$) of those objects without. We would expect a reasonable fraction of the emission-lines to appear in two, rather than one slice, given the spacing and width of the slices. This is true for the line-on-continuum detections. The extreme ratio of one to two-slice candidates for line-only case suggests that many of the one-slice objects could be noise peaks. However, not all are, as Table 8 shows with the comparison to the Autofib data. Only follow-up multi-object spectroscopy can resolve this difficult but crucial issue.

4.3. Number Count and H α Luminosity Function Evolution

In this section we examine the evolution in the number count and volume-averaged star-formation rates of the *TTF Field Galaxy Survey*. From an observational perspective we would like some measure of the density of emission-line sources on the sky. This should comprise all sources with redshifts placing the emission-line within the observed wavelength interval, whatever that emission-line may be. Knowing this quantity is fundamental to optimizing source coverage and maximizing sample size for a volume-limited emission-line survey (Sect. 2). Multi-object spectroscopic follow-up to narrowband samples also requires a knowledge of object densities when deciding between strategies of spectral coverage and slit placement. From the perspective of galaxy evolution, projected number counts potentially provide a strong constraint on evolutionary models, since they comprise galaxies from more than one redshift bin simultaneously. Thus a chosen model must reproduce both the combined numbers observed at each wavelength and the relative mix of H α , [O II], [O III] and other galaxies, all subject to the same evolution. As such, narrowband number counts should provide a stringent test for competing evolutionary models of the star-forming population.

Figure 11 shows the cumulative narrowband number counts from the complete homogeneous sub-sample of the *full* emission-line set (including H α). Sample cuts at 4 and 5 σ demonstrate how the weakest detections influence the counts obtained. The sigma values in this case are the line strengths expressed as a statistical deviation above the background, be it sky or continuum noise. Corrections for incompleteness have been applied to all of the counts shown in Fig. 11. Counts are shown down to the selection limits of the homogeneous sub-sample (Table 5) and the flux cuts for the H α sub-samples are indicated by the dashed lines. Counts are expressed in terms of the projected density of emission-line objects on the sky per bin per 100 Å wavelength scan coverage. In this way, we have a useful measure of the object counts obtained in a flux-limited tunable filter survey, in terms of quantities directly observed. Note that the 100 Å is *not* the scan interval (as given by column 2 of Table 2), but rather the product of the effective bandpass and the number

of slices per scan. Also observe that 100 \AA represents a different redshift coverage Δz at the rest wavelength of each major optical emission-line. However, it is fixed for that line, irrespective of the redshift at which it is observed.

The *solid curves* in Fig. 11 show the estimated numbers we should have expected based on evolving $\text{H}\alpha$ luminosity function calculation, of the type detailed in Sect. 2.2. Thus, the number evolution assumes our earlier model constrained by the Gallego *et al.* (1995) and Tresse & Maddox (1998) $\text{H}\alpha$ luminosity functions, namely

$$\begin{aligned} \log \phi^*(z) &= -3.2 + 4.68 \log_{10}(1+z), \\ \log L^*(z) &= 42.15 - 0.25 \log_{10}(1+z), \\ \alpha(z) &= -1.3 - 0.25z. \end{aligned} \tag{8}$$

This is identical to the general form presented in Eqn. (5). These surveys were chosen due to both their spread in redshift and use of galaxy spectra. The contribution from other major emission-lines is calculated by scaling the $\text{H}\alpha$ luminosity function by the appropriate line-ratio (*c.f.* Fig. 2) at the required redshift. Note that this is *not* a model of our observed counts, but a comparison of those we could have expected based on the luminosity functions of the earlier surveys.

Figure 11 shows that the model expected counts (*solid line*) are a fair match to the $\geq 5\sigma$ distributions in the 707/26 and 814/33 intervals. In the 909/40 interval they are a much closer match to the $\geq 4\sigma$ sample. There are two potential contributions to this difference. The most likely is that we are simply less-sensitive to the same type of galaxies at higher redshift, rendering what we detect as 5σ in 707/26 and 814/33, as 4σ in 909/40. A second effect could be that the model constraints at $z \sim 0$ (Gallego *et al.* 1995) and $z \sim 0.2$ (Tresse & Maddox 1998) are insufficient for the extrapolation to $z \sim 0.4$ where $\text{H}\alpha$ is seen in the 909/40 interval. However, there are presently no $\text{H}\alpha$ -selected galaxy surveys that encompass $z \sim 0.4$.

Observe also in Fig. 11 the significant excess (~ 2 to 3 times) in the faintest narrowband number counts over the comparison with previous surveys (*solid line*). While we have not proven the validity of all detections less than 5σ , our visual confirmation of all line-on-continuum candidates (13%) represents a greater fraction of the total counts than does the *solid line*, at the faintest limits where the difference is largest. This suggests we have an excess in emission-line galaxies over the numbers we would otherwise estimate from these two previous $\text{H}\alpha$ surveys. The corollary of this is that the population of faint star-forming galaxies is more numerous than these surveys have found, consistent with the preliminary findings of Gronwall *et al.* (priv. comm.) for a new wide-field $\text{H}\alpha$ -survey at $z \sim 0.08$. Such a scenario is also consistent with our conclusions from the comparisons between the TTF and Autofib samples in Sect. 4.1.

Before interpreting such higher star-formation densities as indicative of the field, we should consider possible sources of contamination. Both active galactic nuclei (AGN) and quasi-stellar objects (QSOs) are potential emission-line sources at non-zero redshift. Like Tresse & Maddox (1998), we have not removed AGN as their influence on the general emission-line population has previously been shown to be small (*i.e.* $\leq 10\%$; Sarajedini *et al.* 1996; Tresse *et al.* 1996). Likewise,

the occurrence of QSOs to be rare against the general star-forming population: $\leq 2 \text{ } \square^{-1}$ from within a typical high- z TTF interval of $\Delta z = 0.1$, using the number-redshift distribution of Boyle, Shanks & Peterson (1988). This is consistent with the wide-field objective prism survey of Smith, Aguirre & Zemelmann (1976) for emission-line objects down to $b_J \lesssim 18$, with 96% as galaxies and 2% as possible QSOs. The most likely sources of Galactic contamination are late-type stars. Boroson *et al.* (1993) in their 5-filter intermediate-band imaging survey using 80 Å bandpasses, attributed ~ 10 to 20% of their *rejected* emission-line candidature to late-type stars. Such stars have strong molecular TiO absorption bands with widths of typically ~ 500 Å. Presumably these spectral variations were difficult to distinguish from genuine line-emission in the broader 80 Å bandpasses used by these authors. However, our narrower bandpasses (~ 20 to 30 Å), the greater number of them (10), and smaller scan interval (200 to 300 Å), argues that we should not be susceptible to this problem in the same way.

Given the unlikelihood of celestial contamination, our data suggest greater numbers of star-forming galaxies than has previously been attributed to the field population. A consequence of this would be higher mean star-formation densities, although without confirmation of our faintest detections through additional observations, we can not quantify the increase. Specifically, follow-up spectroscopy is required to provide independent confirmation of the faintest emission-line detections, in addition to confirmation of the line as H α . Baker *et al.* (2001) have obtained follow-up spectroscopy to a sample of TTF-selected emission-line galaxies in the field of QSO MRC B0450–221 at $z = 0.9$. Of the 5 TTF candidates targetted, 3 were positively identified as emission-line sources, and 1 as a possible emission-line detection. This important result demonstrates the capacity of TTF for detecting faint emission-line sources at high redshift.

A more immediate approach to evolutionary trends is to compare H α luminosity functions directly. Figure 12 shows the luminosity functions of our homogeneous H α sub-samples in each interval for the $\geq 4\sigma$ (*filled circles*) sample. The H α luminosity functions of Gallego *et al.* (1995; *open triangles*) and Tresse & Maddox (1998; *open circles*) are also shown in the relevant redshift interval. All luminosity functions are shown uncorrected for extinction. Poissonian errors derived from the square-root of the galaxy numbers in each bin are shown. For the TTF data, H α fluxes were corrected for the effect of [N II] using the mean flux ratio $\text{H}\alpha/(\text{H}\alpha + [\text{N II}]) = 0.69$, obtained by Tresse & Maddox (1998) for their sample at $z \sim 0.2$. Star-formation rates were derived using the same calibration as adopted by Glazebrook *et al.* (1999), namely

$$\frac{\text{SFR}}{(M_{\odot} \text{ yr}^{-1})} = 7.4 \times 10^{-42} \frac{L_{\text{H}\alpha}}{(\text{erg s}^{-1})} \quad (9)$$

from the Bruzual & Charlot (1996) models with solar metallicity and a Salpeter IMF. No extinction corrections have been applied to the luminosities, although corrections have been made for the effect of the Airy profile on sampling an ensemble of galaxy line fluxes (Jones 1999). We save the derivation of a luminosity function fit for when we have spectroscopic confirmation of the H α sample in hand.

Figure 12(a) demonstrates the excess in our $z = 0.08$ counts over the faint-end of the Gal-

lego *et al.* (1995) distribution by almost an order of magnitude. Much closer agreement exists between our values and those of a preliminary H α luminosity function from the KPNO International Spectroscopic Survey (KISS; Gronwall 2000, priv. comm). Taken together, these results suggest that the Gallego *et al.* survey underestimates the faint-end of the local H α luminosity function, and hence, the star-formation content of the local universe. For the $z = 0.24$ interval (Fig. 12b) we find broad agreement with the H α luminosity function derived by Tresse & Maddox (1998). Due to the volume-limited nature of the survey we have insufficient numbers to define the bright-end “knee” of the distribution. Our measurements at $z = 0.40$ (Fig. 12c) are the first to use H α in the ~ 5 Gyr of lookback time separating the samples of Tresse & Maddox (1998) at $z \sim 0.2$ and Glazebrook *et al.* (1999) at $z \sim 0.9$.

Our preliminary H α luminosity functions argue for an upwards revision of the star-formation content for the local universe. This in turn implies a less-dramatic decline in the cosmic star-formation history than has been shown to date (Tresse & Maddox 1998; Glazebrook *et al.* 1999; Yan *et al.* 1999). However, follow-up spectroscopy is needed to confirm the nature of the H α detections and to correct individual H α fluxes for the effects of extinction and [N II]. Indeed, if many of our sub- 4σ -detections are verified, then the measured excess would be greater.

5. CONCLUSIONS

We now summarize our preliminary findings from a census of the *TTF Field Galaxy Survey* for star-forming galaxies.

1. Using the TAURUS Tunable Filter (TTF), we have obtained a narrowband-selected sample of emission-line galaxies in the field. The survey is composed of 15 scans of 10 narrowband slices covering $0.27 \square^\circ$ on the sky, with 7 of the scans in a 707/26 nm wavelength interval, 5 in 814/33 nm and 3 in 909/40 nm. There are 696 candidates (at the 3σ level or greater) in a homogeneous sub-sample for which we can correct for incompleteness (96.4%). Although some detections (13) are confirmed by the Autofib Galaxy Redshift Survey, the majority exist without separate confirmation. This is required for both checking the validity of detections and correctly identifying the emission-line concerned. The homogeneous sub-sample excludes two of the worst fields, one in each of the 707 and 909 intervals. Through a synthesis of H α luminosity functions and median galaxy emission-line ratios, we estimate the relative occurrence of different emission-lines in our sample. From this we expect our samples to be dominated by H α galaxies in the sub-samples with line fluxes exceeding 1.50, 0.71 and $0.57 \times 10^{-16} \text{ erg s}^{-1} \text{ cm}^{-2}$ for the 707, 814 and 909 intervals respectively. In these flux regimes, we have 660 candidates from the homogeneous sub-sample that we expect to consist mostly of H α galaxies, correctable for the small amount of incompleteness (96.5%) inherent.
2. We find little evidence for strong clustering in either the full emission-line sample or the H α subset. Those of our fields overlapping with the Lidman & Peterson (1996) cluster candidates

did not yield any clear peaks in redshift space. This allows us to rule out clusters in our field sample as seen in emission-lines. It does not, of course, tell us anything about possible clusters outside of our scan intervals but in the same direction on the sky.

3. We compared the detection ability of TTF in finding emission-line galaxies to the broadband-selected Autofib galaxy redshift survey (Ellis *et al.* 1996). Our comparison was made between the [O II] galaxies found in Autofib and the H α galaxies of TTF. There is little overlap between the emission-line samples of the two surveys. For the sky regions that overlap, most of the TTF-selected galaxies are not seen in the Autofib catalogue because they have continua beyond the selection limit of this catalogue. Conversely, TTF misses many of the Autofib emission-line galaxies because they are beyond the comparatively narrow volumes sampled by TTF. For the galaxies in common, TTF detects $b_J \lesssim 21$ galaxies in both line and continuum while fainter galaxies are detected in the line alone. TTF recovered 13 of an expected 18 Autofib emission-line galaxies, although those that were missed may have been due to weaker H α emission than [O II]. The two surveys agree in their continuum and redshift measurements although show scatter in their line flux and equivalent width measures. However, much of this scatter may be due to intrinsic scatter in the correlation of H α and [O II] fluxes. Better insight into the detection rates of the two methods would be gained through a direct comparison concentrating on the same emission-line at wavelengths common to both.
4. The projected density of emission-line galaxies on the sky was compared to what we would have expected from existing measurements of the H α luminosity function. At the faintest limits we find a significant excess in these narrowband number counts, up to 3 times the expected counts at the faintest flux limits of our $\geq 4\sigma$ sample. This excess is also seen when our preliminary H α luminosity functions are compared directly to those of other surveys, in each redshift interval individually. Although the influence of false detections for the line-only candidates is yet to be quantified, our visual confirmation of the line-on-continuum candidates (13%) is consistent with an excess of emission-line candidates. Such an excess is most likely due to our narrowband selection of the sample, which is without precedent for field emission-line galaxies at these redshifts. The greater numbers imply higher star-formation densities than have previously been attributed to these epochs. However, follow-up measurement of the detections is required to quantify this increase.

Multi-object spectroscopic follow-up is necessary for future work on this sample. Such spectra would cover a wider wavelength range than TTF, and as such, would allow us to resolve many of the issues for which we have presently made assumptions. Spectroscopic information would first allow independent confirmation of the line detections and resolve the redshift ambiguity. Furthermore, with spectra we can determine the amount of reddening in individual galaxies through the H α /H β ratio and correct each for such. If the spectra are of sufficiently high spectral resolution, the H α and [N II] lines can be separated, thereby avoiding contamination of the former by the latter. Furthermore, the H α line fluxes could be measured directly from the line which would remove the need for

the bandpass correction. Finally, through an assessment of ratios such as $[\text{N II}]/\text{H}\alpha$ and $[\text{O III}]/\text{H}\beta$ we could identify and reject AGN from our sample of star-forming galaxies (e.g. Veilleux & Osterbrock 1987). Many existing $\text{H}\alpha$ surveys (e.g. Tresse & Maddox 1998; Yan *et al.* 1999) include these emission-line sources, although they occur in small numbers relative to the general star-forming population.

In short, the *TTF Field Galaxy Survey* is a survey for star-forming galaxies is largely unprecedented in its systematic narrowband search for field galaxies. Our data suggest galaxy counts and mean star-formation rates higher than those measured by previous $\text{H}\alpha$ and UV surveys. An intriguing possibility for the higher values we observe is a population of faint star-forming galaxies, with continua sufficiently faint to place them beyond the range of conventional redshift surveys. However, follow-up measurements utilizing multi-object spectroscopy are required for this to be confirmed.

It is a pleasure to thank Matthew Colless for many helpful discussions regarding this work. We are also grateful to the referee Caryl Gronwall for her reading of the original manuscript and the many improvements that resulted from her suggestions. The comments of the referees who examined this work during its presentation for a Doctoral Thesis are also gratefully appreciated. We acknowledge the Australian Time Allocation Committee for their support of the TTF observations at the AAT upon which this work is based. This research has made use of the NASA/IPAC Extragalactic Database (NED), which is operated by the Jet Propulsion Laboratory, Caltech, under contract with NASA. DHJ acknowledges the support of an Australian Postgraduate Research Award during the completion of this work.

REFERENCES

- Baker, J. C., Hunstead, R. W., Bremer, M. N., Bland-Hawthorn, J., Athreya, R. A. and Barr, J. 2001, submitted
- Bertin, E. and Arnouts, S. 1996, *A&A* 117, 393
- Bland-Hawthorn, J. and Jones, D. H. 1998a, *PASA*, 15, 44
- Bland-Hawthorn, J. and Jones, D. H. 1998b, in *Optical Astronomical Instrumentation*, Proc. SPIE 3355, ed. S. D’Odorico, 855
- Bland-Hawthorn, J., van Breugel, W., Gillingham, P. R., Baldry, I. K. and Jones, D. H. 2001, *AJ* submitted
- Boroson, T. A., Salzer, J. J. and Trotter, A. 1993, *ApJ* 412, 524
- Boyle, B. J., Shanks, T. and Peterson, B. A. 1988, *MNRAS* 235, 935
- Broadhurst T. J., Ellis, R. S. and Shanks, T. 1988, *MNRAS* 235, 827
- Bruzual, A. G. and Charlot, S. 1996, documentation for the B&C models
- Colless, M., Ellis, R. S., Taylor, K. and Hook, R. N. 1990, *MNRAS* 244, 408
- Colless, M., Ellis, R. S., Broadhurst, T. J., Taylor, K and Peterson, B. A. 1993, *MNRAS* 261, 19
- Ellis, R. S., Colless, M., Broadhurst, T., Heyl, J. and Glazebrook, K. 1996, *MNRAS* 280, 235
- Folkes, S., Ronen, S., Price, I., Lahav, O., Colless, M., Maddox, S., Deeley, K., Glazebrook, K., Bland-Hawthorn, J., Cannon, R., Cole, S., Collins, C., Couch, W., Driver, S. P., Dalton, G., Efstathiou, G., Ellis, R. S., Frenk, C. S., Kaiser, N., Lewis, I., Lumsden, S., Peacock, J., Peterson, B. A., Sutherland, W. and Taylor, K. 1999, *MNRAS* 308, 459
- Gallego, J., Zamorano, J., Aragón-Salamanca, A. and Rego, M. 1995, *ApJ* 455, L1
- Glazebrook, K., Ellis, R., Colless, M., Broadhurst, T., Allington-Smith, J. and Tanvir, N. 1995, *MNRAS* 273, 157
- Glazebrook, K., Blake, C., Economou, F., Lilly, S. and Colless, M. 1999, *MNRAS* 306, 843
- Gronwall, C. 1998, in *Dwarf Galaxies and Cosmology*, eds. T. Thuan *et al.* , Paris: Editions Frontières
- Heyl, J. S., Colless, M., Ellis, R. S. and Broadhurst, T. J. 1997, *MNRAS* 285, 613
- Jones, D. H. 1999, *PhD Dissertation*, The Australian National University
- Kennicutt, R. C., Jr. 1992a, *ApJ* 388, 310

- Kennicutt, R. C., Jr. 1992b, *ApJS* 79, 255
- Kennicutt, R. C., Jr. 1998, *ARA&A* 36, 189
- Koo, D. C. 1999, in *Photometric Redshifts and High Redshift Galaxies*, ASP Conference Series v 191, eds. R. Weymann, L. Storrie-Lombardi, M. Sawicki and R. Brunner, San Francisco, p 3
- Lidman, C. E. and Peterson, B. A. 1996, *AJ* 112, 2454
- Lilly, S. J., Le Fèvre, O., Crampton, D., Hammer, F. and Tresse, L. 1995, *ApJ* 455, 50
- Lissberger, P. H. and Wilcock, W. L. 1959, *J. Opt. Soc. Amer.*, 49, 126
- Metcalfe, N., Shanks, T., Fong, R. and Roche, N. 1995, *MNRAS* 273, 257
- Peterson, B. A., Ellis, R. S., Bean, A. J., Efstathiou, G. P., Shanks, T., Fong, R. and Zou, Z-L. 1985, *MNRAS* 221, 233
- Phillips, M. M., Jenkins, C. R., Dopita, M.A., Sadler, E. E. and Binette, L. 1986, *AJ* 91, 1061
- Rhoads, J. E., Malhotra, S., Dey, A., Stern, D., Spinrad, H. and Jannuzi, B. T. 2000, preprint, (astro-ph/0003465)
- Salzer, J. J., Gronwall, C., Lipovetsky, V. A., Kniazev, A., Moody, J. W., Boroson, T. A., Thuan, T. X, Izotov, Y. I., Herrero, J. L., Frattare, L. M. 2000, *AJ* 120, 80
- Sandage, A. and Tammann, G. A. 1981, *A Revised Shapley-Ames Catalog of Bright Galaxies*, (Washington DC: Carnegie Institution of Washington)
- Sarajedini, V., Green, R. F., Griffiths, R. E. and Ratnatunga, K. 1996, *ApJ* 471, L15
- Sarajedini, V., Green, R. F., Griffiths, R. E. and Ratnatunga, K. 1999, *ApJ* 514, 746
- Schechter, P. 1976, *ApJ* 203, 297
- Smith, M. G., Aguirre, C. and Zelman, M. 1976, *ApJS* 32, 217
- Tresse, L., Rola, C., Hammer, F., Stasińska, G., Le Fèvre, O., Lilly, S. J. and Crampton, D. 1996, *MNRAS*, 281, 847
- Tresse, L. and Maddox, S. J. 1998, *ApJ* 495, 691
- Tresse, L., Maddox, S. J., Loveday, J. and Singleton, C. 1999, *MNRAS* 310, 262
- van der Werf, P. P. 1997, in *Extragalactic Astronomy in the Infrared*, eds. G. A. Mamon, Trinh Xuan Thuan and J. Tran Thanh Van, Paris: Editions Frontières, 451
- Veilleux, S. and Osterbrock, D. E. 1987, *ApJS* 63, 295

Yan, L., McCarthy, P. J., Freudling, W., Teplitz, H. I., Malumuth, E. M., Weymann, R. J. and Malkan, M. A. 1999, ApJ 519, L47

Zamorano, J., Rego, M., Gallego, J., Vitores, A. G., González-Riestra, R. and Rodríguez-Caderot, G. 1994, ApJS 95, 387

Table 1. Scan Parameters

Filter $\lambda/\Delta\lambda$ (nm)	Range of Central Wavelengths (\AA)	Passband FWHM (\AA)	Effective Passband (\AA)	Step size (\AA)
707/26	6986–7183	12.9	20.3	21.9
814/33	8026–8263	16.4	25.8	26.3
909/40	8945–9245	22.3	35.1	33.4

Table 2. Narrowband Scan Coverage

Filter $\lambda/\Delta\lambda$ (nm)	Redshift Range ($z_1 \leq z \leq z_2$)	\bar{z}	Proper Distance (Mpc ³)	δv ^a (km s ⁻¹)	No. of Fields	Total Volume (Mpc ³)	$\log(L_{\text{line}})$ ^b (erg s ⁻¹)	SFR ^{bc} (M_{\odot} yr ⁻¹)
H α line:								
707/26	$0.062 \leq z \leq 0.093$	0.077	438	8610	7	1170	39.43	0.02
814/33	$0.221 \leq z \leq 0.260$	0.24	1230	9510	5	6660	40.44	0.22
909/40	$0.359 \leq z \leq 0.411$	0.39	1800	11200	3	9850	40.87	0.59
[O II] line: ^d								
707/26	$0.870 \leq z \leq 0.924$	0.90	3290	8610	7	49500	41.67	6.57
814/33	$1.149 \leq z \leq 1.219$	1.18	3880	9510	5	50300	41.93	12.14
909/40	$1.393 \leq z \leq 1.484$	1.44	4320	11200	3	42500	42.12	18.73

Assuming $H_0 = 50 \text{ km s}^{-1} \text{ Mpc}^{-1}$ and $q_0 = 0.5$. Circular TTF field of $9'$ diameter.

^avelocity coverage per field in the rest frame of the emission-line sources, $\delta v = c(z_2 - z_1)/(1 + \bar{z})$.

^bH α or [O II] log line luminosity at a detected flux of $1 \times 10^{-16} \text{ erg s}^{-1} \text{ cm}^{-2}$.

^cstar-formation rate using $\text{SFR} (M_{\odot} \text{ yr}^{-1}) = L_{\text{H}\alpha}/10^{41.10} = L_{[\text{O II}]}/10^{40.85}$, with luminosities expressed in (erg s⁻¹), excluding internal galactic extinction.

^dnot as prevalent as H α at the flux limits of the survey.

Table 3. *TTF Field Galaxy Survey: Log of Observations*

Field	R. A. (J2000) (h m s)	Dec. (J2000) (° ′ ″)	Number of Slices	Exposure Time (s slice ⁻¹)	Observation Date	Autofib Galaxies ^a
707/26 scans:						
00_3A	00 54 48.0	−30 25 00	9	600	1997 Oct 08	2
10_3F	10 45 18.0	−00 05 00	10	600	1997 May 01	–
10_3D	10 45 42.0	−00 15 00	10	620	1998 Apr 04	2
12_3A	12 44 18.0	−00 07 00	10	600	1997 May 01	–
13_3E	13 44 12.0	−00 01 00	10	600	1998 Apr 04	2
14_3A	14 45 30.0	+00 05 00	10	400	1997 Apr 30	–
			10	+200	1997 May 01	–
22_3A	22 05 10.9	−18 35 00	10	400	1997 Apr 30	–
			10	+200	1997 May 01	–
814/33 scans:						
01_3A	01 05 48.0	−30 00 00	9	600	1997 Oct 08	1
13_3C	13 43 27.0	−00 20 00	10	620	1997 Apr 30	2
13_3B	13 44 04.8	−00 22 00	10	600	1998 Apr 05	2
13_3E	13 44 12.0	−00 01 00	10	600	1998 Apr 04	2
14_3A	14 45 30.0	+00 05 00	10	600	1997 May 01	–
909/40 scans:						
10_3C	10 44 30.0	−00 07 00	9	1080	1998 Apr 05	–
10_3H	10 46 24.0	−00 24 00	10	1080	1998 Apr 03	2
13_3D	13 44 42.0	−00 11 30	10	1080	1998 Apr 03	3

^aEmission-line galaxies from the Autofib survey (Ellis *et al.* 1996) with (1) redshifts placing H α within the scan interval, and, (2) [O II] rest-frame equivalent widths ≥ 10 Å.

Table 4. H α Luminosity Function Evolution

Luminosity Function at $z = 0$	Evolutionary Indices
$\phi_0^* = 0.63 \times 10^{-3} \text{ Mpc}^{-3}$	$\gamma_\phi = 4.68$
$L_0^* = 10^{42.15} \text{ erg s}^{-1}$	$\gamma_L = -0.25$
$\alpha_0 = -1.3$	$\gamma_\alpha = -0.25$

Table 5. Selection Limits of Homogeneous Sub-Sample

Filter $\lambda/\Delta\lambda$ (nm)	Flux ($\text{erg s}^{-1} \text{cm}^{-2}$)	Central Surface Brightness ^a ($\text{erg s}^{-1} \text{cm}^{-2} \square''$)	EW (\AA)	REW in H α (\AA)
707/26	1.2×10^{-16}	0.031×10^{-16}	2.2	2.0
814/33	0.71×10^{-16}	0.031×10^{-16}	4.0	3.2
909/40	0.57×10^{-16}	0.031×10^{-16}	4.0	3.3

^aAssuming an exponential disk profile

Table 6. Homogeneous Sub-Sample

Filter $\lambda/\Delta\lambda$ (nm)	Line-only Objects	Line-on-Continuum Objects	Total No. Observed	Total No. Expected	Completeness ^a (%)
707/26	75	30	105	111.89	93.8
814/33	387	36	423	431.76	98.0
909/40	141	27	168	178.42	94.2
Overall:	603	93	696	722.07	96.4

^aover the entire homogeneous sub-sample in each filter

Table 7. H α Sub-Samples From Full and Homogeneous Sets

Filter (nm)	Limiting H α Flux (erg s $^{-1}$ cm $^{-2}$)	$\log L(\text{H}\alpha)^{\text{a}}$ (erg s $^{-1}$)	From Homog. Sub-sample	No. Expected (Completeness)
707/26	1.50×10^{-16} ^b	39.61	69	74.05 (93.2%)
814/33	0.71×10^{-16} ^c	40.30	423	431.76 (98.0%)
909/40	0.57×10^{-16} ^c	40.67	168	178.42 (94.2%)
Overall:			660	684.22 (96.5%)

^aLimiting H α luminosity (erg s $^{-1}$).

^bflux cut placed higher than that of the original homogeneous sub-sample

^cidentical flux cut to that of the original homogeneous sub-sample; *i.e.* homogeneous sub-sample consists entirely of H α candidates.

Table 8. TTF Detection of Autofib Sub-Sample

Range	TTF Detections ^a	Undetected	Line-Only	Line-on- Continuum
By b_J magnitude:				
$18.0 \leq b_J < 19.0$	1/1	0	0	1
$19.0 \leq b_J < 20.0$	4/4	0	1	3
$20.0 \leq b_J < 21.0$	4/5	1	1	3
$21.0 \leq b_J < 22.0$	3/7	4	2	1
$22.0 \leq b_J < 23.0$	1/1	0	1	0
By [O II] EW:				
$EW \geq 60 \text{ \AA}$	1/2	1	0	1
$50 \leq EW < 60 \text{ \AA}$	0/1	1	0	0
$40 \leq EW < 50 \text{ \AA}$	1/1	0	0	1
$30 \leq EW < 40 \text{ \AA}$	5/6	1	1	4
$20 \leq EW < 30 \text{ \AA}$	1/2	1	0	1
$10 \leq EW < 20 \text{ \AA}$	5/6	1	4	1

^anumber detected by TTF out of the number of Autofib galaxies available

Table 9. Emission-Line Occurrence in Homogeneous Sub-Sample

Filter $\lambda/\Delta\lambda$ (nm)	Line-Only 1 Slice	Line-Only 2 Slices	Line-on-Continuum 1 Slice	Line-on-Continuum 2 Slices
707/26	75	0	15	15
814/33	381	6	23	13
909/40	138	3	14	13
Total:	594	9	52	41

Fig. 1.— Distribution of survey regions on the sky. Regions are labeled with the number of fields contained in each. Control fields (*triangles*) are randomly chosen high galactic latitude regions. The remaining fields (*circles*) were deliberately chosen to overlap with Autofib Survey galaxies. The north and south galactic poles (NGP/SGP) are also indicated (*crosses*).

Fig. 2.— Evolution of the mean Kennicutt (1992a) line-flux ratios with redshift. All ratios are expressed relative to $(\text{H}\alpha + [\text{N II}])$ (*solid lines*) except $[\text{N II}]$ which is shown relative to $\text{H}\alpha$ alone (*dashed line*). Change in the ratios is due to the weighting of the Kennicutt sample by the numbers of galaxy type found at each redshift (*inset*). Galaxy densities are taken from the evolution of $\phi^*(z)$ for individual galaxy types as given by Heyl *et al.* (1997).

Fig. 3.— Predicted relative occurrence of emission-line galaxies in each of the three wavelength regions of the *TTF Field Galaxy Survey*. Shown are the relative numbers per flux bin (*left*) and the cumulative numbers to fainter limiting flux (*right*).

Fig. 4.— (*top*) Example strip-mosaic scans of a subset of candidates from a *TTF Field Galaxy Survey* field. Individual images are $9''$ on a side with north at top, east to the left. Circles denote aperture size. (*bottom*) TTF spectra for the same galaxies. Preliminary (*dotted line*) and final (*solid line*) continuum fits. Numbers shown (*right*) are flux ($\times 10^{-16}$ ergs $^{-1}$ cm $^{-2}$ band $^{-1}$), star-galaxy classification parameter and σ -deviation. Deviant points (excluded from the final continuum fit) are also indicated (*circles*). The zero flux level is shown by the horizontal tickmarks (where present) and non-detections are represented on this level (*crosses*). Galaxy 214.14 is one of the 18 Autofib objects in common with our fields. All of these objects are taken from a field observed in the 707/26 interval.

Fig. 5.— (*a*) Distribution of σ -deviations for the preliminary catalogue of emission-line candidates selected with σ -deviation ≥ 3 . Line-only (*horizontal tickmarks*) and line-on-continuum detections (*crosses*) are shown separately and the fields are grouped according to blocking filter spectral locations (707, 814 or 909 nm). (*b*) Distributions of σ -deviations across all fields pertaining to the 707 (*solid*), 814 (*dotted*) and 909 (*dashed*) filters. (*c*) Cumulative distributions of those shown in (*b*).

Fig. 6.— (*left*) Line-only candidates shown in terms of both mean detected (emission-line) flux and object size (full-width at half-maximum, FWHM), for each of the 707/26, 814/33 and 909/40 emission-line samples. The 22_3A (707) and 10_3C (909) candidates have been removed. The detection probability contours (*solid lines*) indicate levels of 20, 40, 60 and 80% and are taken from the *single least-sensitive* field in each group. All other fields have contours at fainter limits (not shown). The 60% contour is highlighted (*bold line*). (*right*) Same sample of line-only candidates with the chosen cuts of line flux and surface brightness overlaid. Members of the homogeneous sub-sample lie above these two lines.

Fig. 7.— (*left*) Line-on-continuum candidates shown in terms of both mean detected (continuum) flux and object size (full-width at half-maximum, FWHM), for each of the 707/26, 814/33 and 909/40 emission-line samples. The 22_3A (707) and 10_3C (909) candidates have been removed. Identical flux and surface brightness cuts to those applied to the line-only sample in Fig. 6 are also shown (*solid lines*). (*right*) Same sample of line-on-continuum objects showing the scatter of continuum flux and emission-line flux. The flux cuts applied at *left* have also been applied here to both the line and continuum (*vertical and horizontal lines*). The detection probability contours (*solid lines*) indicate levels of 20, 40, 60 and 80% and are taken from the *single least-sensitive* field in each group. All other fields have contours at fainter limits (not shown). The 60% contour is highlighted (*bold line*). Lines showing the cut in observed equivalent width are shown labeled with their respective values (*solid diagonal line*). The *dotted line* shows the limiting locus for 3σ -deviation objects as measured through the largest aperture.

Fig. 8.— Cumulative completeness of the homogeneous sub-samples in the (a) 707/26, (b) 814/33 and (c) 909/40 filters, in the limit of fainter flux.

Fig. 9.— Comparison between Autofib and TTF flux measurements, with the measurements from each plotted on the abscissa and ordinate of each panel. (a) TTF-measured ($\text{H}\alpha + [\text{N II}]$) line fluxes against Autofib $[\text{O II}]$ equivalent widths. (b) TTF-measured ($\text{H}\alpha + [\text{N II}]$) equivalent widths against those of $[\text{O II}]$ from Autofib. The row of points along the top denote galaxies detected by TTF for which the equivalent width was indeterminable. (c) TTF-measured continuum flux versus b_J photographic magnitude. The best-fit $b_J = -2.5 \log F(\text{cont}) + 21.81$ is also shown (*dotted line*), weighted by the $1/\Delta F^2$ continuum photometry uncertainties.

Fig. 10.— Redshift distributions as measured from the subset of $\text{H}\alpha$ emission-line candidates. Distributions shown for each field in the (a) 707/26, (b) 814/33, and (c) 909/40 sets.

Fig. 11.— Narrowband number counts for the homogeneous sub-sample of emission-line candidates above the 4 (*filled circles*) and 5σ (*open circles*) limits of survey selection. Shown are cumulative numbers in each of the 707/26, 814/33 and 909/40 sets. All counts are expressed in terms of the total object number per flux bin, per square degree of sky, per 100 \AA of scan interval. Counts have been corrected through the incompleteness weights derived in Sect. 3.2. Flux bins are $0.1 \log[F(\text{H}\alpha)]$ and the flux limits for each of the $\text{H}\alpha$ sub-samples (forming only *part* of these sets) are also shown (*vertical dotted lines*). The *solid line* shows evolution constrained by the Gallego *et al.* (1995) and Tresse & Maddox (1998) $\text{H}\alpha$ luminosity functions, as detailed in Sect. 2.2.

Fig. 12.— Preliminary $\text{H}\alpha$ luminosity functions from the *TTF Field Galaxy Survey* (*filled circles*) at mean redshifts of (a) $\bar{z} = 0.08$, (b) $\bar{z} = 0.24$, and (c) $\bar{z} = 0.4$. No extinction corrections have been applied to the luminosities. The other points are the $\text{H}\alpha$ luminosity functions from Gallego *et al.* (1995; *open triangles*) for $z \lesssim 0.045$ and Tresse & Maddox (1998; *open circles*) at $z \sim 0.2$.

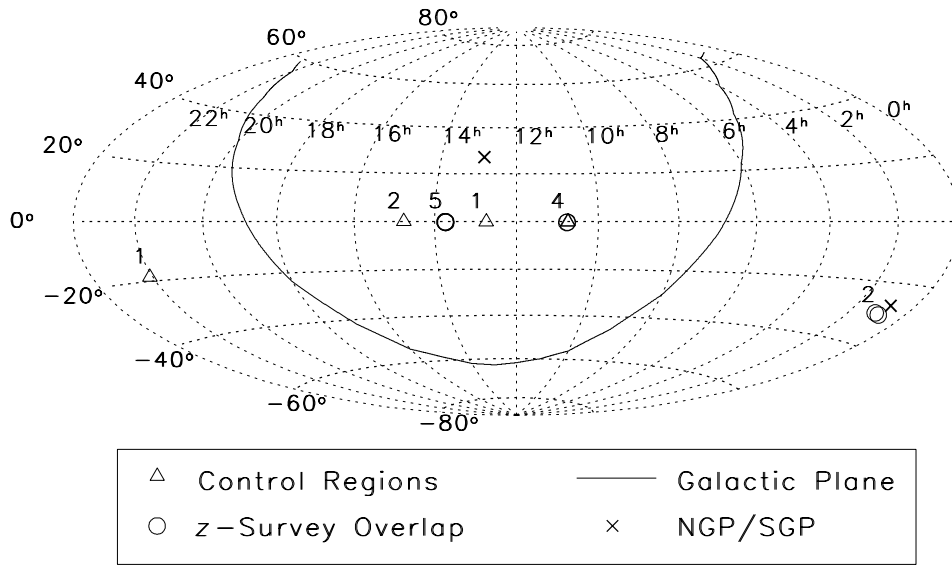


Figure 1

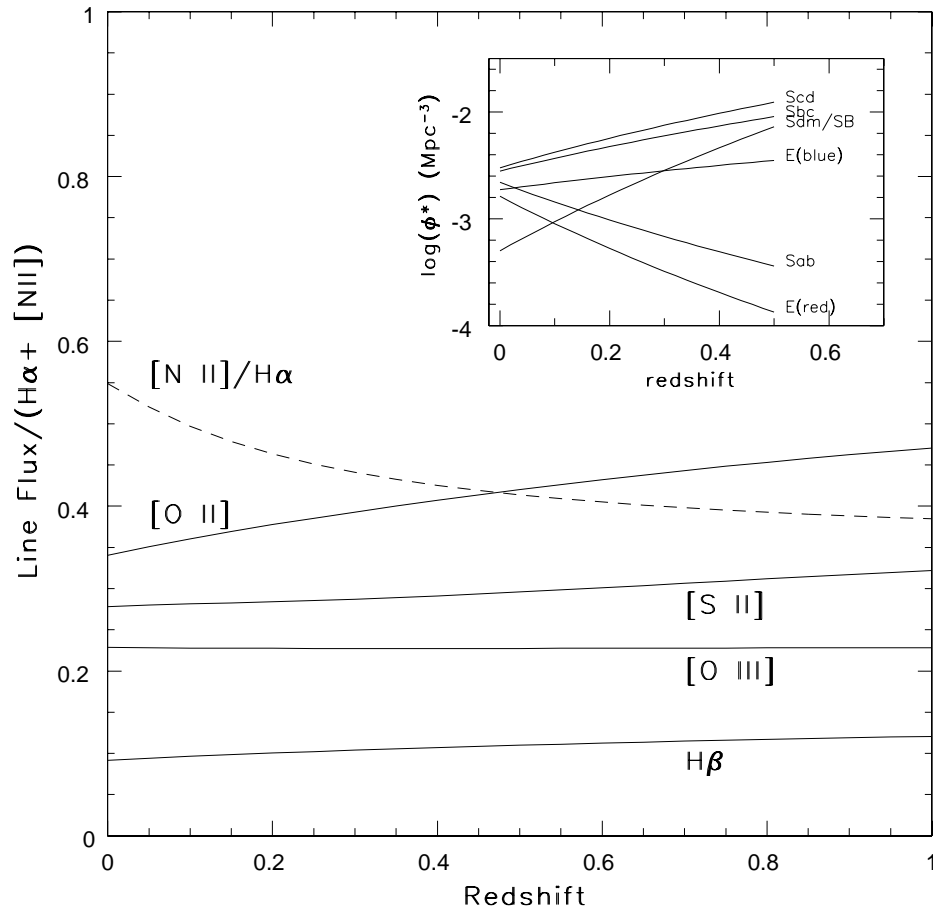


Figure 2

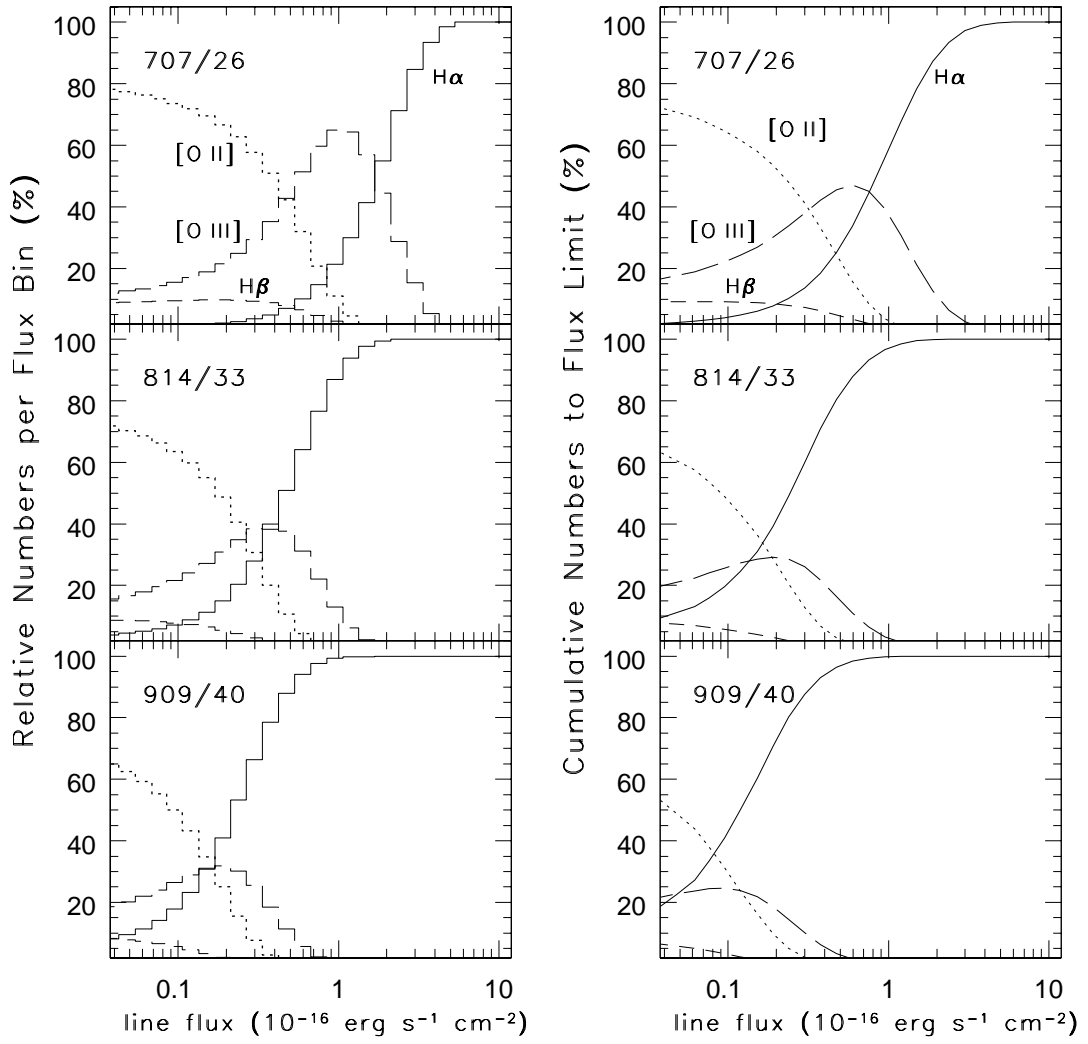


Figure 3

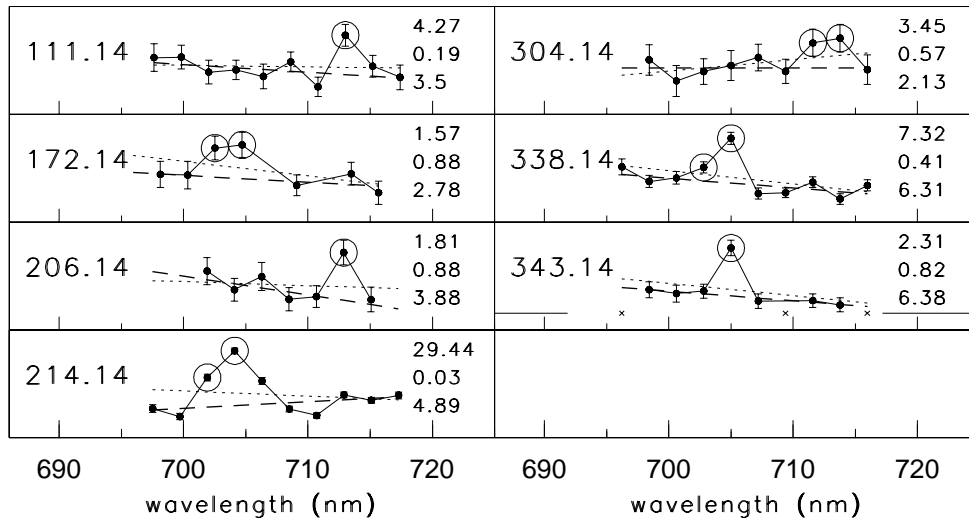
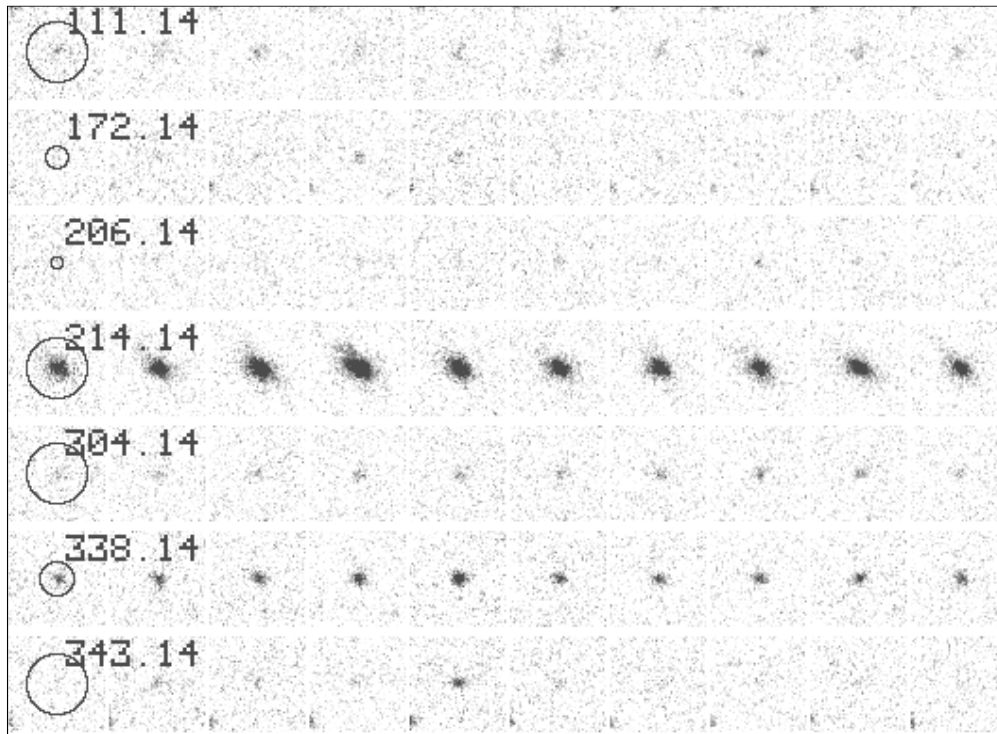


Figure 4

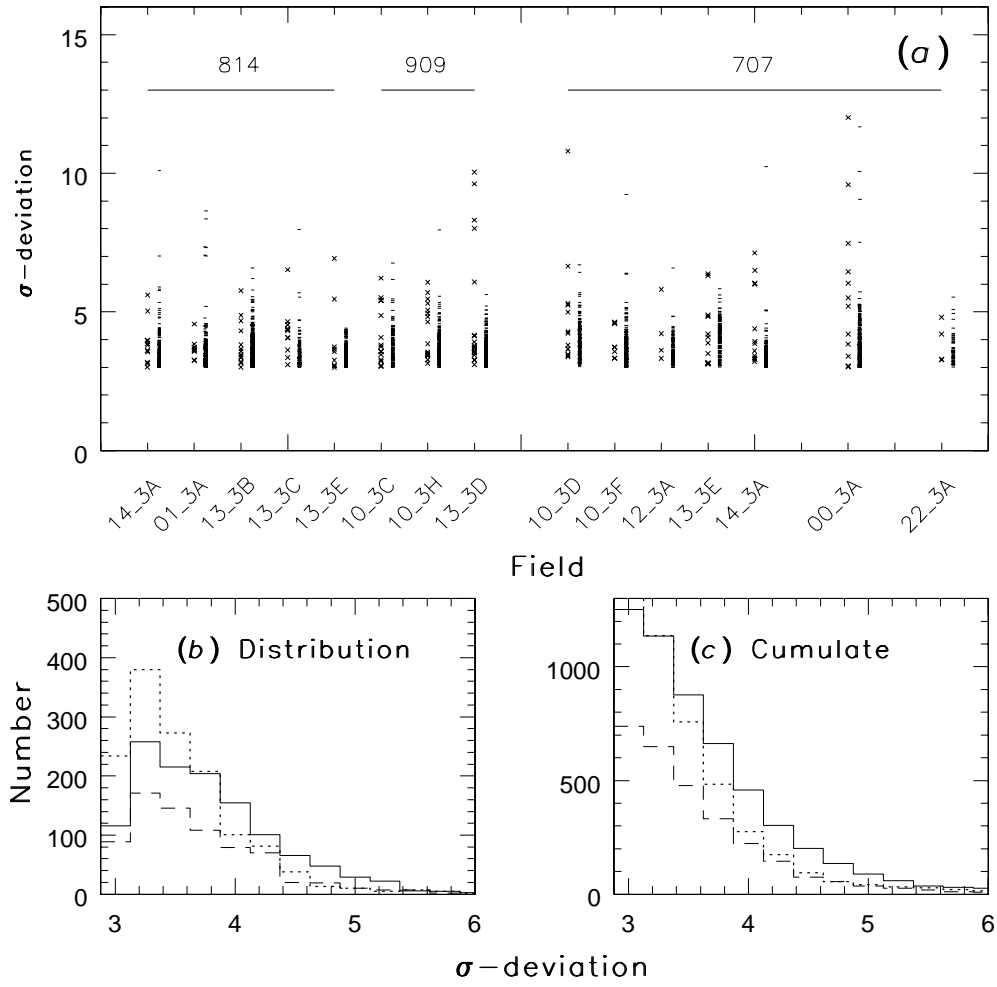


Figure 5

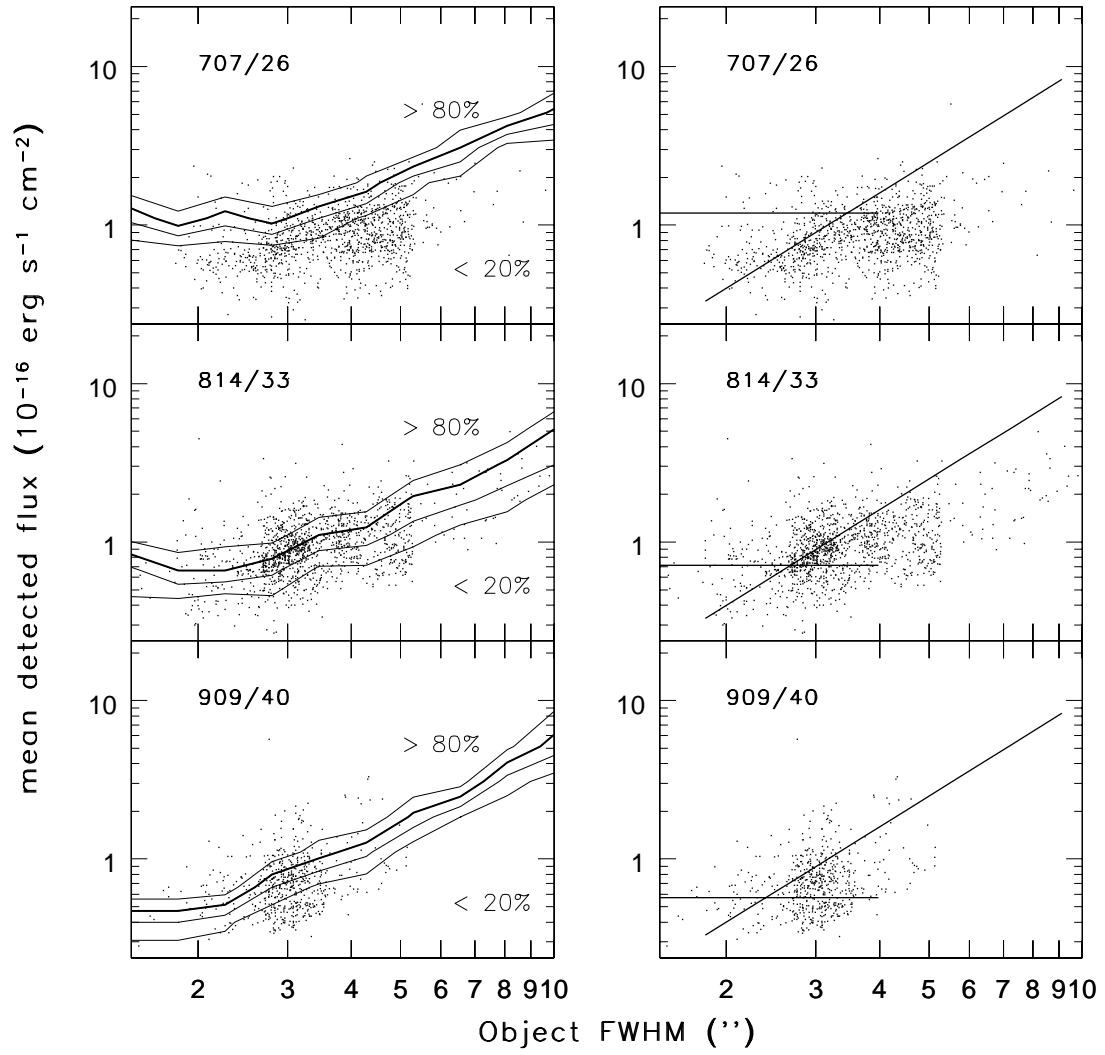


Figure 6

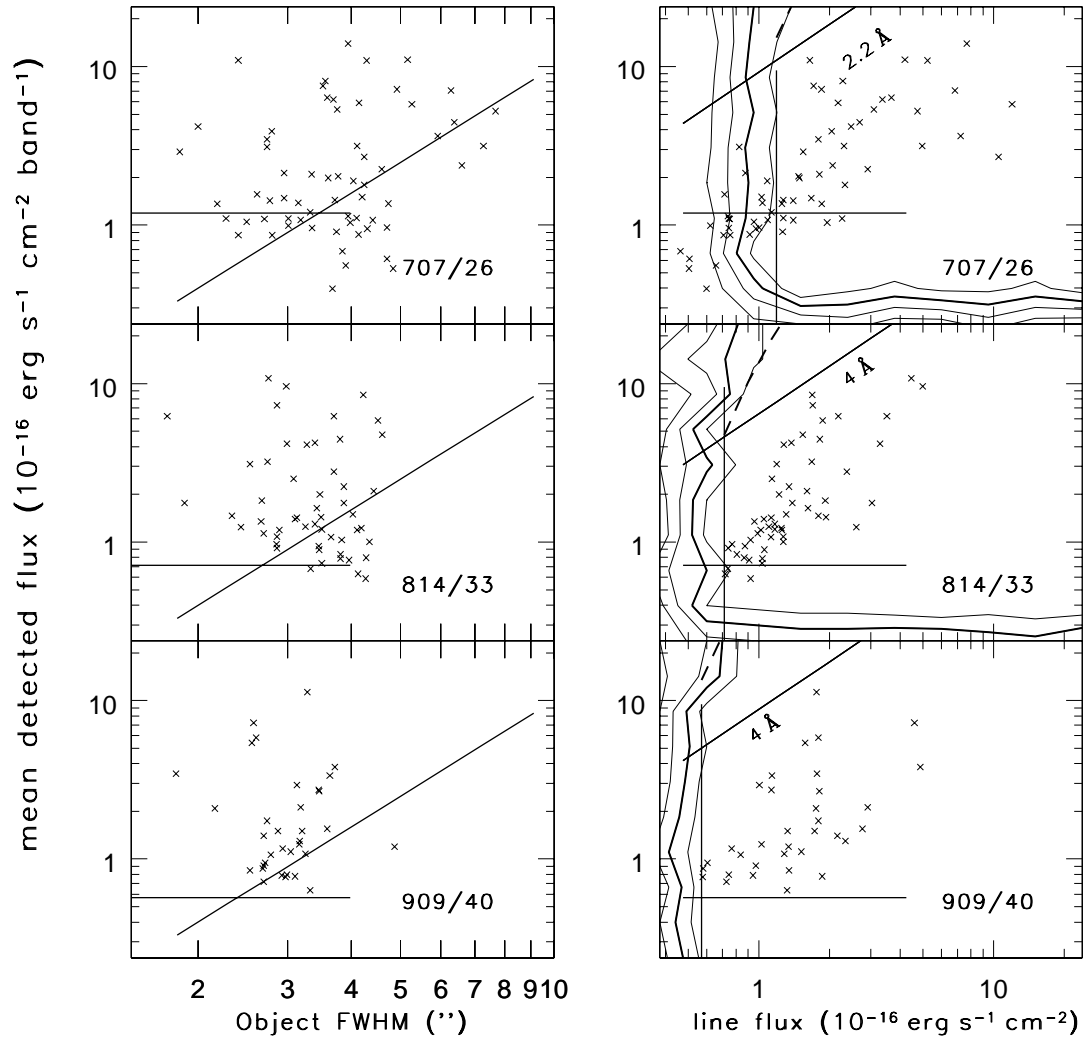


Figure 7

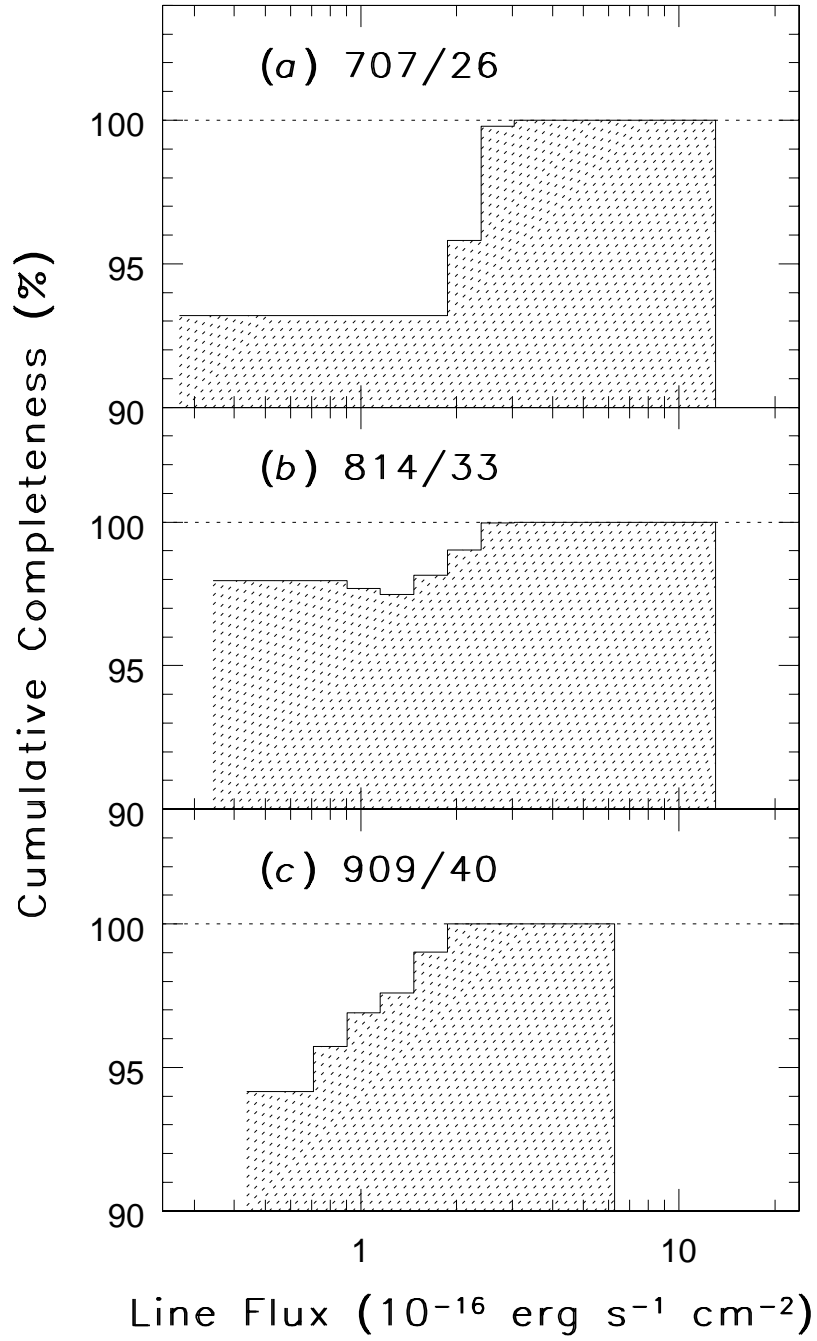


Figure 8

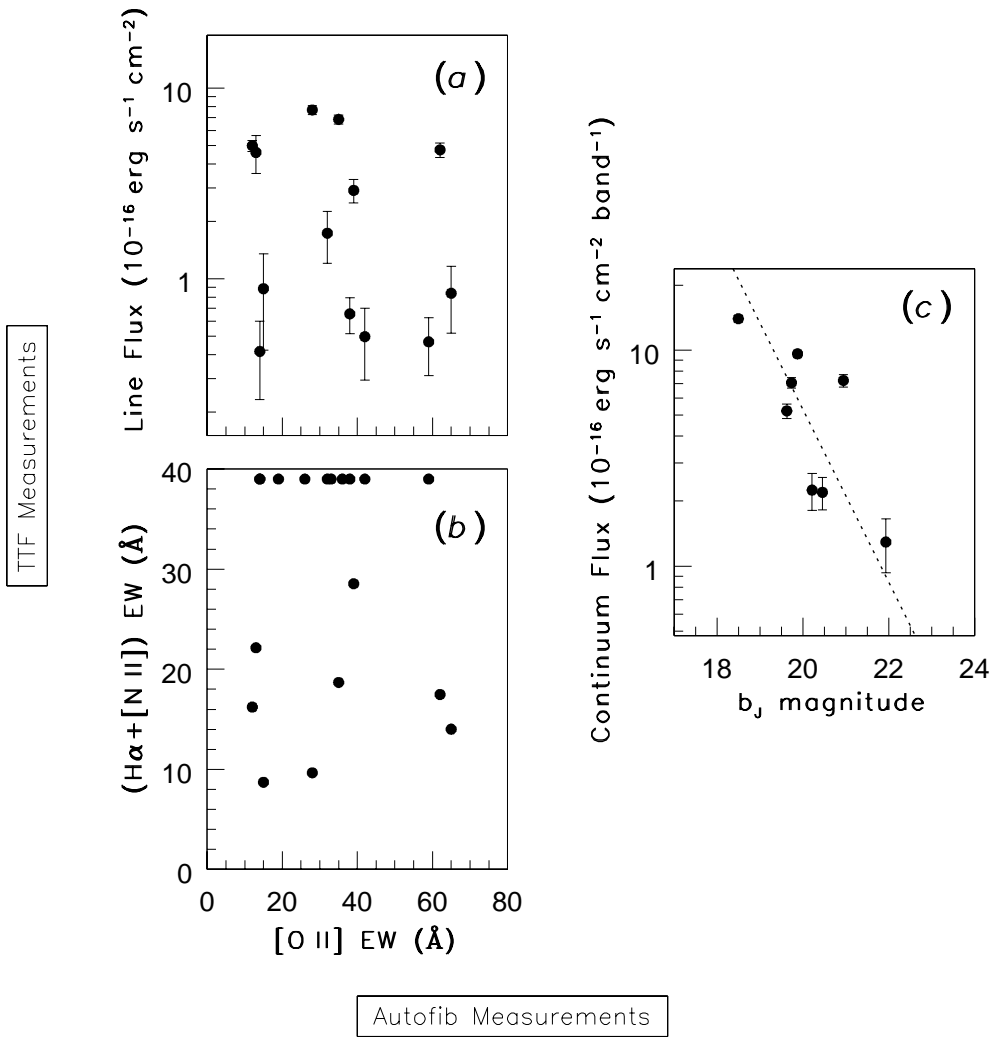


Figure 9

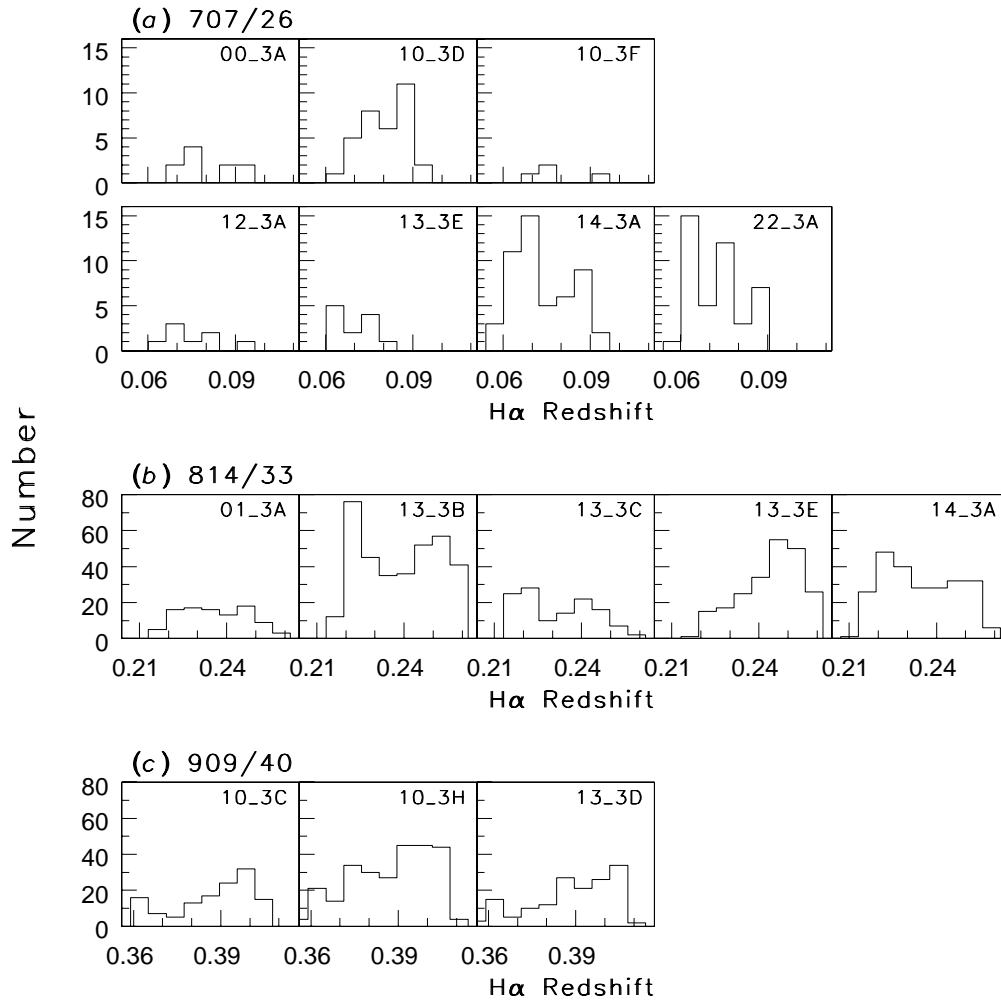


Figure 10

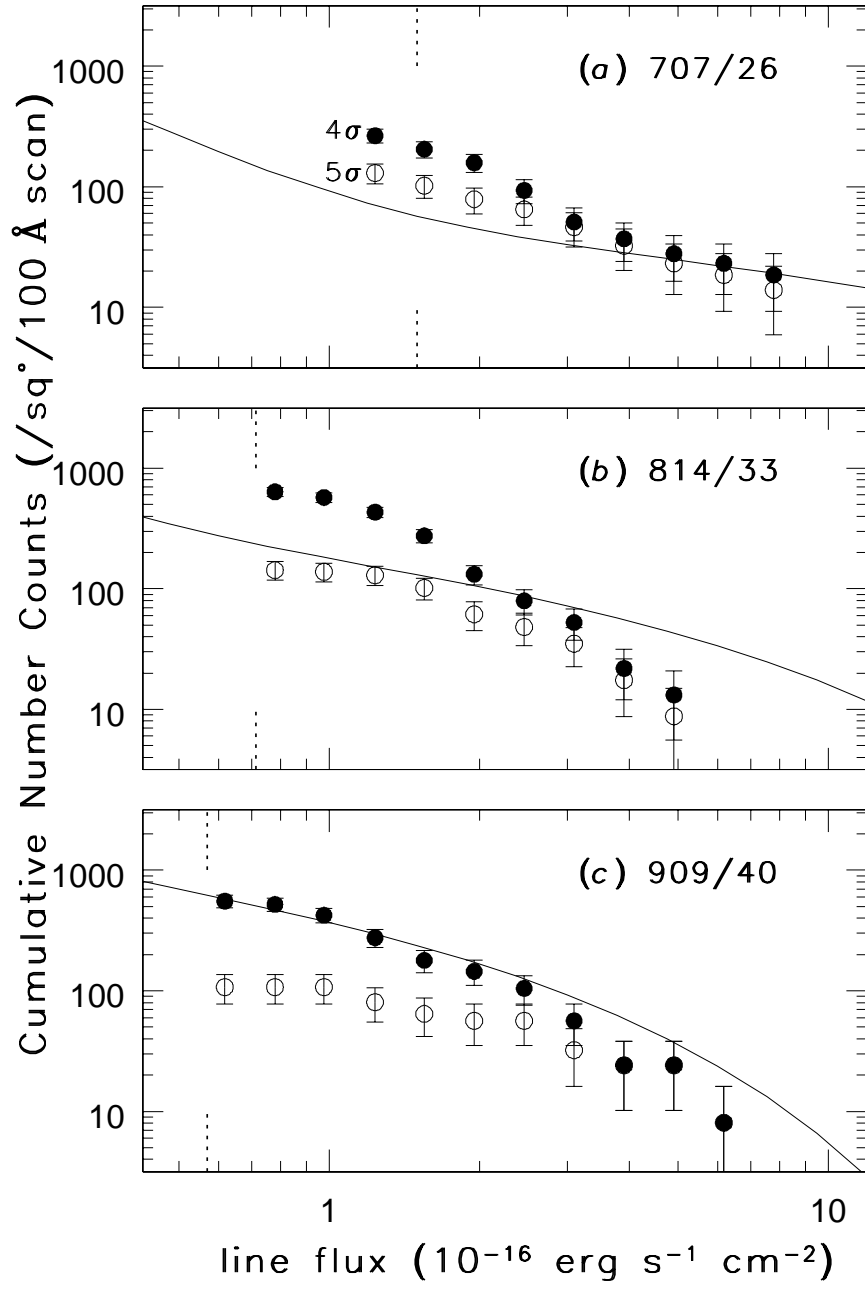


Figure 11

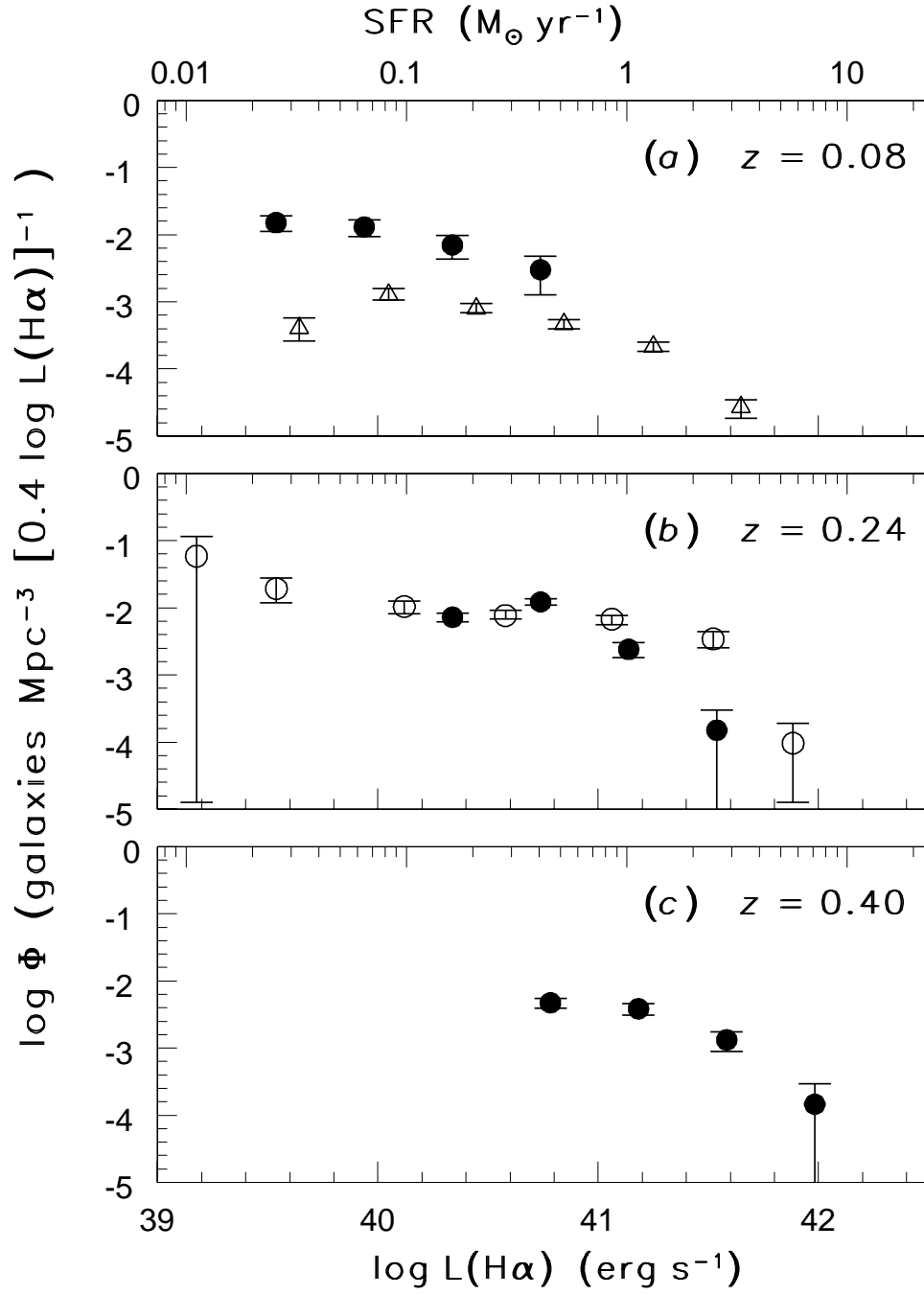


Figure 12